(U-Th)/He thermochronology of metallic ore deposits in the Liaodong Peninsula: Implications for orefield evolution in northeast China

Yinzhi Wang[a,c,*], Fei Wang[a,b], Lin Wu[a], Wenbei Shi[a], Liekun Yang[a]

[a] State Key Laboratory of Lithospheric Evolution, Institute of Geology and Geophysics, Chinese Academy of Sciences, Beijing 100029, China
[b] CAS Center for Excellence in Tibetan Plateau Earth Sciences, China
[c] University of Chinese Academy of Sciences, Beijing 100049, China

A B S T R A C T

The Liaodong Peninsula is an important region where polymetallic ores are mined in northeast China, but precise thermochronological data needed to effectively constrain the evolution of this orefield are presently lacking. For this study, fifteen samples of granitoid rocks were collected from the Qingchengzi and Wulong orefields located in the Liaodong Peninsula to undertake (U-Th)/He study of zircon and apatite. Single-grain ZHe and AHe ages from the Qingchengzi orefield range from 73 to 166 Ma and from 22 to 48 Ma, respectively, whereas single-grain ZHe and AHe ages from the Wulong orefield range from 42 to 88 Ma and from 21 to 56 Ma, respectively. Some samples yield dispersed ages. Comprehensive analyses indicate that the main causes of the dispersion in the ZHe ages are heterogeneous distribution of U and Th within the crystals, radiation damage and cooling rates, whereas the dispersion in the AHe ages is primarily due to the first two factors. Based on the helium ages, we calculate the average exhumation and cooling rates of the two orefields during different periods and the associated denudation, which are 4.3 km for the Qingchengzi orefield and 4.7 km for the Wulong orefield. The mineralization depths are estimated using homogenization temperature and the salinity of fluid inclusions, and are calculated to be 1.5–3.2 km and 1.0–2.2 km for the Qingchengzi Pb-Zn and Au-Ag deposits, respectively, and 2.1–3.1 km for the Wulong Au deposit. These results are much less than the total denudation, suggesting that the orebodies have been heavily eroded. In conjunction with the distribution of the helium ages, the modeled low-T thermal histories of the two orefields reveal that the Liaodong Peninsula experienced three stages of relatively rapid cooling during the Early Cretaceous (ca. 135–115 Ma), from the end of the Late Cretaceous to the Early Eocene (ca. 70–50 Ma) and from the Late Eocene to the Oligocene (ca. 38–26 Ma). The last stage of cooling affected both orefields and represents a period of relatively intense tectonic activity. Finally, these results are compared with those of previous studies from the adjacent Jiaodong Peninsula. This discussion shows that the cooling experienced by the orefields in the Liaodong Peninsula is largely consistent with that experienced by the Jiaodong Peninsula. These data provide valuable information for further studies of the evolution of orefields in northeast China.

1. Introduction

The Liaodong Peninsula in northeast China is an important region where polymetallic ores are mined, including Pb-Zn, Au, Ag, Mo and Fe. Most studies have focused on the metallogenic mechanism and age (Jiang and Wei, 1989; Liu and Ai, 2002; Xue et al., 2003; Liu et al., 2007; Yu et al., 2009; Wang et al., 2010a; Duan et al., 2012, 2014), while little attention has been paid to their thermal histories. Moreover, the Liaodong Peninsula is located between the two deep faults- the Yalujiang and Tan-Lu fault zones (Fig. 1b) – and experienced complex geological events (Chen, 1995; Li et al., 2000, 2004; Guo et al., 2005;

Wan et al., 2013), during which its orebodies may be heavily transformed. So it is crucial to explore the thermal evolution of the ore deposits in the Liaodong Peninsula since their formation, as this analysis can provide information on the exhumation and erosion histories in the ore-hosting terranes. Moreover, the study of detailed thermal histories is of great importance for understanding of the ore distribution, preservation and exposure of ore deposits (Zhai et al., 2000; McInnes et al., 2005; Wang et al., 2008; Fu et al., 2010; Li et al., 2014; Yang et al., 2015).

The tectonic activities of post-mineralization mostly comprised low-temperature deformation, which usually cannot be identified using U-

---
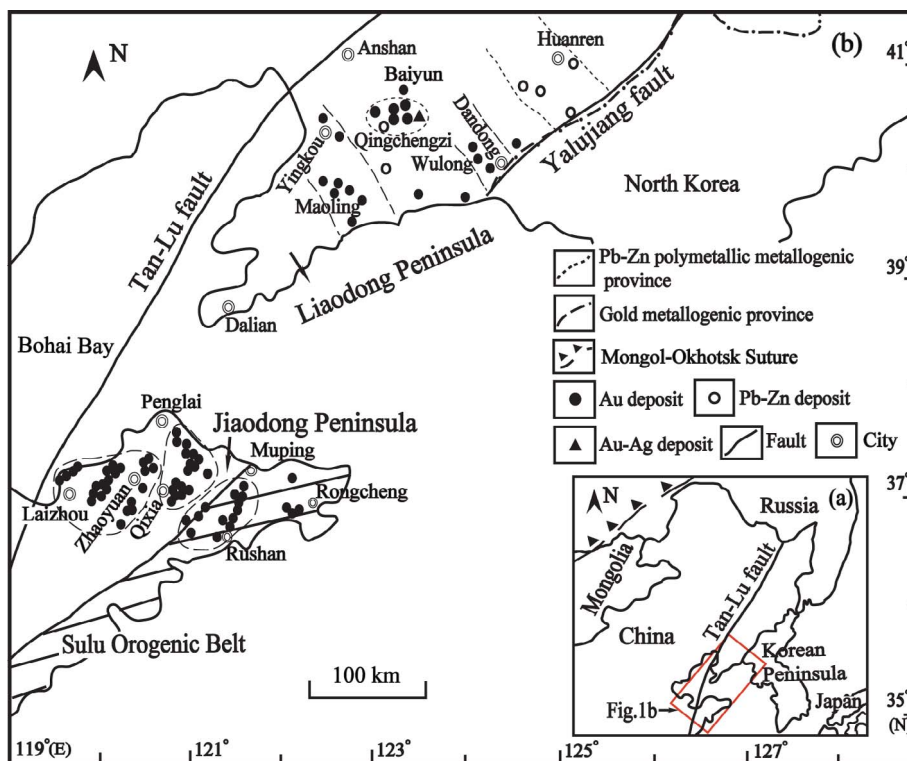
Pb or ^{40}Ar/^{39}Ar methods, due to the relatively high closure temperatures of these isotopic systems (i.e., 350–900 °C, Zeitler, 1985; Sang et al., 1992; Scott and Stonge, 1995; Kooijman et al., 2009; Scharf et al., 2016). In contrast, zircon and apatite (U-Th)/He methods, which can reveal the cooling histories of rock bodies between temperatures of 160 °C to 200 °C (Reiners et al., 2004) and 40 °C to 85 °C (Wolf et al., 1998), respectively, are powerful tools to study near-surface tectonic activities (Benjamin et al., 1987; Wolf et al., 1997; McInnes et al., 1999; Braun, 2005; Evans et al., 2005; Ding et al., 2007; Chang et al., 2010, 2011; Sun et al., 2015; Wang et al., 2016; Wu et al., 2016). Therefore, the (U-Th)/He system has been widely used as a low-temperature geochronometer to decipher the post-mineralization evolution of ore deposits, including their cooling, denudation and preservation (McInnes et al., 2005; Fu et al., 2010; Betsi et al., 2012; Liu et al., 2014; Li et al., 2014; Yang et al., 2015; Sun et al., 2016).

The Qingchengzi and Wulong orefields are two important mining areas in the Liaodong Peninsula. In this paper, we report zircon and apatite (U-Th)/He ages from the main granitoid intrusions, which are closely related to mineralization in the Qingchengzi and Wulong orefields. We also constrain the detailed cooling and denudation histories of the Liaodong Peninsula using (U-Th)/He methods and explore the evolution and preservation of these polymetallic ore deposits. Moreover, to ensure that the cooling processes revealed by the zircon and apatite (U-Th)/He data resulted from tectonic uplift rather than in situ cooling at shallow depth, the Al-in-hornblende barometer is used to estimate the emplacement depths of these intrusions.

The Jiaodong Peninsula is to the southwest of the Liaodong Peninsula, across the Bohai Bay (Fig. 1b). Many super-large gold deposits (> 50 t), such as Linglong and Jiaojia orefields, have been identified in the Jiaodong Peninsula (total gold reserve of > 4000 t, Yang et al., 2014; Fan et al., 2016). The Liaodong and Jiaodong Peninsulas reveal similar tectonic settings, as both peninsulas are located on the eastern margin of the North China Craton adjacent to the western margin of the Pacific Plate, and they are bounded to the west by the NNE-trending Tan-Lu deep fault zone. However, the gold mineral endowment on the Liaodong Peninsula is much smaller than those on the Jiaodong Peninsula (Qiu et al., 2002; Sun and Sun, 2004; Guo,

2006; Song et al., 2009; Zhang et al., 2012; Li and Shao, 2015; Fan et al., 2016). Consequently, we will discuss the processes of their cooling and exhumation after their formation in conjunction with the previously collected data from adjacent area of the Jiaodong Peninsula. These data are potentially essential for better understanding of the evolution of polymetallic ore in northeast China.

2. Geologic setting

2.1. The Qingchengzi orefield and sampling

The Qingchengzi orefield is a host to Pb-Zn ores, which are distributed within the Zhenzigou, Xiquegou, Nanshan and Benshan mining areas. The Au-Ag ores occur along its periphery, including the Xiaotongjiapuzi and Gaojiapuzi mining areas (Fig. 2a). The Qingchengzi orefield is an important site for Pb-Zn-Au-Ag resources in northeast China; it contains an estimated 1.5 Mt of Pb and Zn metals, 1100 t of Ag metal and 200 t of Au metal.

The Qingchengzi orefield occurs within the Paleoproterozoic Liaodong rift zone, which is an intracontinental rift that developed within the Archean North China Craton via crustal extension, rapid subsidence, and compressional folding during the Paleoproterozoic (Fang et al., 1994; Zhao and Sun, 1997). The Paleoproterozoic successions of the Liaohe Group were deposited between 2.1 and 1.9 Ga, followed by metamorphism at ca. 1.85–1.9 Ga (Sun et al., 1993; Luo et al., 2004, 2008; Chen et al., 2005; Wan et al., 2006). The Liaohe Group is further divided into three formations. At the bottom is the Langzishan Formation, which contains graphitic marble, hornblende schist and wollastonite mica schist. At the top, the Gaixian Formation consists of mica schist and wollastonite mica schist. Between these formations, the Dashiqiao Formation consists of dolomitic marble, banded mica marble, tremolite marble, garnet mica schist and wollastonite mica schist. Stratiform, veined and irregularly developed massive Pb-Zn deposits occur primarily in the Dashiqiao Formation, whereas Au-Ag deposits are primarily hosted by the Gaixian Formation (Liu et al., 2000, 2007; Wang et al., 2010a; Liu et al., 2013; Duan et al., 2014).
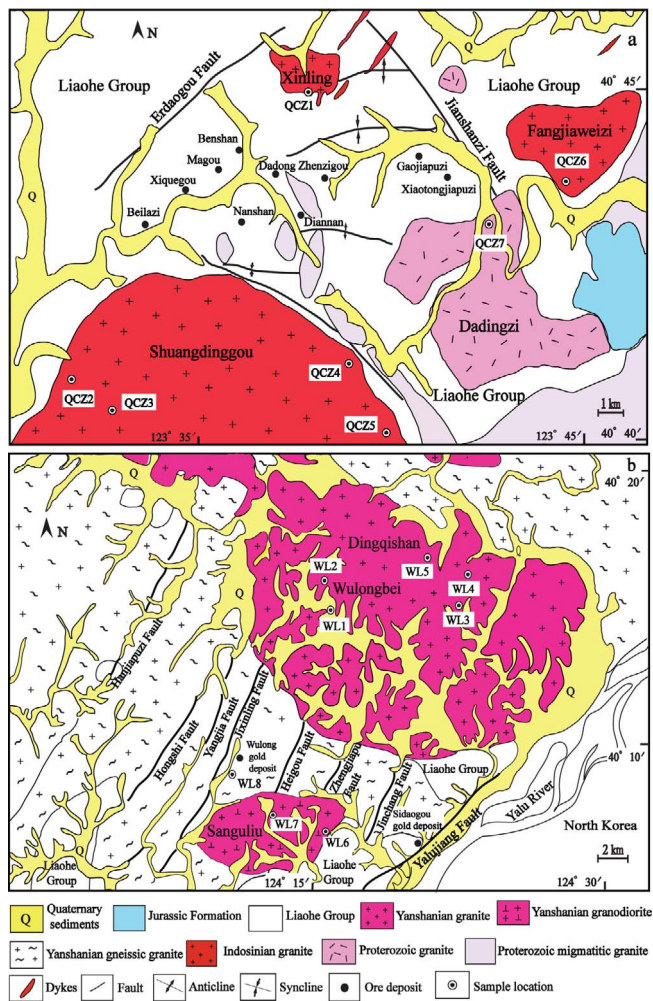
Fig. 2. (a) Geological map of the Qingchengzi orefield (from the regional geological map of Liaoning Province, 1975) showing the locations of samples used for (U-Th)/He dating. (b) Geological map of the Wulong orefield (from the regional geological map of Liaoning Province, 1974) showing the locations of samples used for (U-Th)/He dating.

Geologically, two NE- and NW-striking fault zones cross-cut the Liaohe Group and control the spatial distribution of the ore deposits. For instance, almost all Au-Ag mineralization occurs along the NW-trending Jianshanzi fault. In addition, several E-W-trending folds have formed in the Paleoproterozoic metamorphic rocks, some of which were deformed into overturned folds (Liu, 1995; Wang et al., 2010a; Ban, 2010).

There are extensive multi-phase granitoids in the Qingchengzi area (Fig. 2a). These plutons can be divided into three complexes: (1) the Proterozoic Dadingzi plagiogranite; (2) the Upper Triassic Shuang-dinggou biotite monzogranite and Xinling granite, and (3) the Middle Jurassic Yaojiagou granite (Rui et al., 1994; Zhao and Sun, 1997; Liu et al., 2000; Ban, 2010). Of these units, the Shuangdinggou plutons occupy larger areas than the other plutons. Gravimetric data show that granitoids are the dominant lithology throughout the orefield (Fang et al., 1994; Wang et al., 2010a). Moreover, previous studies indicated that a three-phase magmatism that occurred primarily during the Mesozoic was closely related to this mineralization. This magmatism represents a strong thermal event that activated and reconcentrated metals, forming the orebodies (Liu and Ai, 2002; Xue et al., 2003; Yu et al., 2009; Wang et al., 2010a).

Seven samples for zircon and apatite (U-Th)/He dating were collected from outcrops of the granitoid rocks distributed throughout the orefield. Sample QCZ1 was collected from the Xinling granite; samples QCZ2, QCZ3, QCZ4 and QCZ5, which are made up of biotite

monzogranite, were collected from the Shuangdinggou granitoid; sample QCZ6 was collected from the Fangjiaweizi pluton; and sample QCZ7 was collected from the Proterozoic Dadingzi plagiogranite. The locations and lithologies of all of the samples are shown in Fig. 2a.

2.2. The Wulong orefield and sampling

The Wulong orefield mainly include the Wulong and Sidaogou gold deposits. The Wulong gold deposit, located approximately 30 km west of Dandong in Liaoning Province, is a large, quartz vein-type gold deposit, and it has produced more than 80 t of gold. The mineralization age of this deposit mainly ranges from 112 to 120 Ma (Wei et al., 2001, 2003, 2004). Systematic analysis of fluid inclusions in the auriferous quartz veins suggests that the Wulong gold deposit is a medium-to-high-temperature magmatic hydrothermal deposit (Xiao et al., 2003; Wang et al., 2010b).

The Liaohe Group occurs sporadically among the widespread intermediate to acidic plutons (Fig. 2b). The Yanshanian monzogranite, which has a U-Pb age of 163 ± 7 Ma (Wu et al., 2005) and records gneissic textures, is the host rock of gold ore. The Sanguliu granodiorite, the Dingqishan porphyritic biotite granite and the Wulongbei por-phyritic granite yielded U-Pb isotopic ages of 129 ± 3 Ma, 121 ± 1 Ma and 126 ± 1 Ma, respectively (Wu et al., 2005). Many studies suggested that Yanshanian magmatic activity played a crucial role in the mineralization at the Wulong gold deposit (Xiao et al., 2003; Wei et al., 2004; Liu et al., 2010). Diorite, granite porphyry, lampro-phyre and diabase porphyrite dykes are widespread within the mining area.

Location of the Wulong gold deposit is mainly controlled by fractures. Within the orefield, brittle fractures are widespread. The major NE-trending Yalujiang fault, a first-order structure in the region, is characterized by multi-stage activities (Xia and Xu, 1993; Zhang et al., 2006). A set of approximately parallel and regularly spaced NNE-trending faults on the western side of the Yalujiang fault represent the second-order structure in the region. From the east to the west, the Jinchang, Zhengjiapu, Heigou, Jixinling, Yangjia, Hongshi and Han-jiapuzi faults were mapped (Fig. 2b). Considerable amounts of fault gouge and structural lenses of distinct lithologies, such as fine-grained diorite and auriferous quartz veins, occur within these faults and may reflect different stages of evolution. The Jixinling fault is the closest to the Wulong gold deposit and is an important ore-bearing structure. The ore-bearing structures within the orefield comprise a lattice pattern formed by NS- and NW-trending faults produced during the sinistral shearing along the Jixinling fault. The distribution of the gold orebodies correlates with the distributions of auriferous quartz veins and dikes containing fine-grained diorite and granite porphyry (Xiao et al., 2003; Ji, 2009; Liu et al., 2010).

The orebodies confined to the nearly N-S- and NW-trending faults are mainly vein-like and lenticular in shape and are spatially related to the fine-grained diorite dikes. The ore minerals are primarily pyrite, pyrrhotite, bismuthinite, native gold, chalcopyrite, sphalerite and electrum; the gangue minerals are dominated by quartz, sericite, chlorite, calcite and fluorite. Silicification, pyritization, sericitization, chloritization and carbonatization are the main alteration types of wall rocks. Based on hand specimen analysis and field investigation, the Wulong gold deposit could be formed during four main metallogenic stages: 1. the coarse-grained pyrite-quartz stage; 2. the pyrite-bis-muthinite-quartz stage; 3. the polymetallic sulfide-quartz stage; and 4. the quartz-carbonate stage (Wei et al., 2001, 2003, 2004; Xiao et al., 2003; Wang et al., 2010b; Liu et al., 2010).

To perform zircon and apatite (U-Th)/He dating, eight samples (WL1, WL2, WL3, WL4, WL5, WL6, WL7 and WL8) were mainly collected from the Sanguliu, Dingqishan, and Wulongbei plutons, with small number of samples collected from other plutons in the orefield. The locations and lithologies of these samples are shown in Fig. 2b.
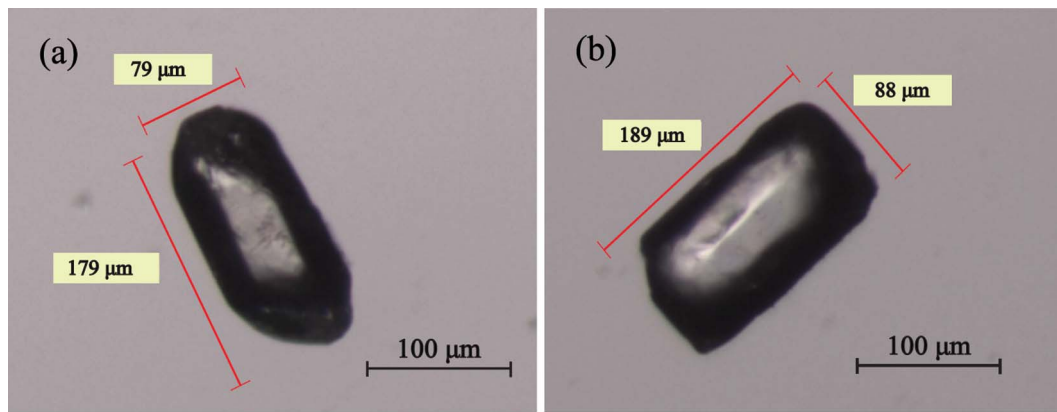
Fig. 3. Microscope photos of zircon and apatite selected for the (U-Th)/He dating: (a) QCZ2-z1, (b) QCZ2-a1. Two grains are free of impurities, inclusions and internal fractures, and exceed 60 μm in width.

3. Methodology

3.1. (U-Th)/He method

3.1.1. Analytical techniques

All of the samples collected from the two orefields were analyzed using the (U-Th)/He dating method. All of the measurements were performed at the (U-Th)/He Laboratory of the Institute of Geology and Geophysics, Chinese Academy of Sciences (IGGCAS). After crushing and heavy liquid separation, zircon and apatite grains were handpicked under a high-power microscope; euhedral crystals that were free of impurities, inclusions and internal fractures were selected. In addition, grains that exceeded 60 μm in width were preferentially selected (Fig. 3). The sizes of the selected grains were then measured precisely to enable calculation of the α calibration factor (F_T). Subsequently, each zircon and apatite grain was enclosed within a 1 mm × 1 mm Nb-Pt capsule and prepared for the U, Th and He analyses.

3.1.1.1. Zircon.
An Alphachron MK II, a fully automatic He extraction system produced by Australian Scientific Instruments Pty, Ltd. (ASI), was used to measure the He in the zircon grains. This system consists of a 970-nm diode laser, a fully automatic gas purification line, and a quadrupole mass spectrometer. The zircon grains were placed into a stainless-steel disk that was heated to a high temperature of 1200 °C for 15 min using the diode laser; this procedure allowed extracting more than 99% of the ^{4}He from the samples. A replicate extraction was then performed to ensure that complete outgassing of ^{4}He had been achieved. The gas, which was purified by two SAES AP-10-N getters, was measured using a Quadrupole Prisma Plus QMG 220. The abundances of ^{4}He were determined using the isotope dilution method, for which a pure ^{3}He spike that was calibrated daily against an independent ^{4}He standard tank was employed. The uncertainty in the ^{4}He measurements was less than 2%. The degassed zircon crystals were removed from the steel disk and placed into a Parrish-type vial, to which 25 μL of the spike solution (containing 15 ppb ^{235}U and 15 ppb ^{230}Th) and 350 μL of HF were added. The spiked samples, blanks (including a Nb blank containing a Nb capsule similar to that used for the samples) and 25 μL of a standard solution (containing 25 ppb U and 25 ppb Th), including 25 μL of the spike solution and a Nb capsule, were then placed into the Teflon liner of the Parr bomb. Ten millilitres of dilute HF and 420 μL of lower-grade HNO$_3$ were then added to the Teflon liner of the Parr bomb. The Parr bomb was then sealed and heated to 240 °C for 36 h. Once the bomb had cooled to room temperature, the acid was evaporated on a hot plate for 48 h. To redissolve the precipitated fluoride salts and ensure the full recovery of U and Th, 350 μL of HCl was added to each Parrish vial, 9 mL of HCl was added to the Teflon liner, and the bomb was reheated to 200 °C for

24 h. Finally, the contents of the vials were transferred to 2-mL Teflon vials and evaporated until 50 μL of solution remained. Three hundred microliters of Milli-Q H$_2$O were then added, and the solution was prepared for the analysis of U and Th in a Thermo Fisher X-Series II ICP-MS. Based on the averages of replicate analyses of the spiked standard solutions, the analytical precisions of the measured ^{235}U/^{238}U and ^{230}Th/^{232}Th ratios were 0.8% and 0.5%, respectively. In this study, we obtained an average age of 29.9 ± 1.8 Ma for the FCT zircon standard, which is in agreement with the results obtained by other laboratories (Tagami et al., 2003; Reiners and Nicolescu, 2006).

3.1.1.2. Apatite.
The procedures that were used in the extraction and analysis of ^{4}He in apatite are similar to those of zircon, which are described in detail in Section 3.1.1.1. The main difference in these procedures is that the apatite was heated to 850–900 °C for 5 min. After ^{4}He extraction, apatite-bearing platinum capsules were transferred to PFA beakers. A total of 25 μL of spike solution (stored in 7 mol/L HNO$_3$), which contained 15 ng/mL U and 5 ng/mL Th (^{235}U/^{238}U = 838 ± 7, ^{230}Th/^{232}Th = 10.45 ± 0.05), was added to each vial. Simultaneously, a set of standard solutions containing the same amount of spike as the samples and non-spiked reagent blanks were treated similarly. To completely dissolve the apatite, the PFA beakers were first ultrasonically washed for 15 min. After remaining at room temperature for at least 4 h to ensure full dissolution, the solution was diluted to 350 μL with Milli-Q water prior to the of U and Th measurements. The instrument used and the analytical precision are the same as those described above for zircon. Analysis of the Durango apatite, which was used as a standard to monitor the analytical procedure, yielded an average age of 33.8 ± 0.8 Ma, which is consistent with the ages obtained by other laboratories (McDowell et al., 2005; Reiners and Nicolescu, 2006).

3.1.2. Results
The results of the (U-Th)/He analyses of the zircon and apatite grains from the 15 samples are summarized in Tables 1 and 2. The average ages exclude those from grains that were rejected.

3.1.2.1. The Qingchengzi orefield.
Sample QCZ1 was collected from the Xinling granite, and seven apatite and four zircon grains were analyzed from this sample. The four zircons have a narrow range of Th/U ratios (0.4–0.5) and got ZHe ages ranging from 122.6 ± 7.2 to 133.4 ± 7.6 Ma, with an average age of 128.1 ± 4.4 Ma. The seven apatite AHe ages range from 30.8 ± 1.6 to 86.9 ± 4.6 Ma, five of which yielded a mean age of 39.0 ± 6.7 Ma (i.e., QCZ1-a3, QCZ1-a4, QCZ1-a5, QCZ1-a6, and QCZ1-a7; QCZ1-a1 and QCZ1-a2 got older ages).

Samples QCZ2, QCZ3, QCZ4 and QCZ5 are biotite monzogranite and

Table 1
Zircon and apatite (U-Th)/He ages for the samples from the Qingchengzi orefield.

	Sample	Mass (ug)	Radius[c] (um)	U (ppm)	Th (ppm)	Th/U	eU[a] (ppm)	He (nmol/g)	Ft[b]	Raw age (Ma)	± σ (Ma)	Cor age (Ma)	± σ (Ma)
Xinling	QCZ1												
	Zircon												
	QCZ1-z1	3.8	44.0	758.2	296.5	0.4	827.9	445.6	0.77	99.63	3.49	129.1	7.9
	QCZ1-z2	2.0	33.5	861.3	319.0	0.4	936.3	465.6	0.72	92.11	2.53	127.4	7.3
	QCZ1-z3	2.5	33.0	824.2	359.5	0.5	908.7	487.1	0.74	99.22	2.77	133.4	7.6
	QCZ1-z5	3.8	36.0	605.0	262.5	0.4	666.7	344.9	0.78	95.78	2.94	122.6	7.2
	Apatite												
	QCZ1-a1[*]	2.2	44.0	12.2	61.6	5.2	26.7	7.7	0.68	53.39	1.1	78.5	4.3
	QCZ1-a2[*]	1.6	39.0	17.7	88.9	5.2	38.5	11.8	0.65	56.22	1.05	86.9	4.6
	QCZ1-a3	1.2	36.0	18.4	93.5	5.3	40.2	4.5	0.62	20.4	0.43	33.1	1.8
	QCZ1-a4	2.3	38.0	14.8	55.4	3.9	27.7	4.6	0.66	30.69	0.58	46.3	2.5
	QCZ1-a5	1.6	35.0	13.1	56.1	4.4	26.2	3.8	0.63	26.49	0.54	41.9	2.3
	QCZ1-a6	1.3	32.5	18.3	82.8	4.7	37.6	5.3	0.61	25.86	0.52	42.7	2.3
	QCZ1-a7	2.0	35.0	13.7	64.2	4.9	28.7	3.1	0.64	19.69	0.37	30.8	1.6
Shuangdinggou	QCZ2												
	Zircon												
	QCZ2-z1	7.1	35.5	435.2	241.0	0.6	491.9	274.9	0.82	103.37	3.62	125.6	7.7
	QCZ2-z2	3.8	42.5	696.6	378.3	0.6	785.6	410.0	0.77	96.59	3.33	125.3	7.6
	QCZ2-z3	1.8	31.0	599.4	348.9	0.6	681.4	320.3	0.71	87.06	1.95	122.3	6.7
	QCZ2-z5[*]	3.2	35.0	301.8	161.9	0.6	339.8	149.9	0.76	81.75	1.75	107.0	5.8
	Apatite												
	QCZ2-a1	2.2	44.5	11.9	55.8	4.8	25.0	2.8	0.68	20.64	0.44	30.3	1.6
	QCZ2-a2	1.3	34.5	14.1	68.2	5.0	30.0	3.6	0.62	21.95	0.44	35.6	1.9
	QCZ2-a3	2.1	38.0	14.3	58.6	4.2	27.9	3.8	0.66	25.39	0.46	38.5	2.0
	QCZ2-a4	0.9	33.5	8.6	43.2	5.2	18.7	1.5	0.59	14.98	0.41	25.5	1.5
	QCZ2-a5	1.4	32.5	13.1	65.8	5.2	28.5	3.3	0.61	21.49	0.44	35.2	1.9
	QCZ2-a6	1.2	32.5	14.2	79.1	5.8	32.7	3.0	0.60	17.07	0.44	28.5	1.6
	QCZ3												
	Zircon												
	QCZ3-z1	7.2	46.0	470.9	232.9	0.5	525.6	316.3	0.82	111.26	4.79	135.7	9.0
	QCZ3-z2	2.2	31.0	580.4	339.8	0.6	660.2	338.9	0.73	95.01	2.35	129.4	7.2
	QCZ3-z3	3.0	38.5	674.2	411.0	0.6	770.8	419.6	0.76	100.72	2.41	133.4	7.4
	QCZ3-z4	1.6	33.0	814.8	414.3	0.5	912.1	492.0	0.70	99.83	2.12	142.6	7.8
	QCZ3-z5	2.0	30.0	498.4	313.6	0.7	572.1	319.2	0.73	103.2	2.2	141.8	7.7
	Apatite												
	QCZ3-a1	2.2	38.0	15.8	77.6	5.1	33.9	4.0	0.66	21.84	0.4	33.2	1.8
	QCZ3-a2	2.1	36.5	16.4	82.8	5.2	35.7	4.5	0.65	23.08	0.44	35.6	1.9
	QCZ3-a3	2.3	33.5	9.8	49.5	5.2	21.4	2.0	0.63	17.23	0.36	27.3	1.5
	QCZ3-a4	1.2	36.0	11.6	55.4	4.9	24.6	2.1	0.62	15.74	0.37	25.6	1.4
	QCZ3-a5	1.3	32.5	10.5	47.8	4.7	21.7	2.0	0.60	17.38	0.41	28.8	1.6
	QCZ3-a6	1.2	34.0	13.3	56.4	4.4	26.5	2.5	0.61	17.16	0.3	28.1	1.5
	QCZ5												
	Zircon												
	QCZ5-z1	2.3	32.5	521.2	347.7	0.7	603.0	336.4	0.74	103.18	2.33	140.4	7.7
	QCZ5-z2	2.1	34.0	800.8	320.6	0.4	876.1	384.3	0.73	81.31	1.96	111.8	6.2
	QCZ5-z3	1.8	28.5	583.9	340.7	0.6	663.9	358.9	0.72	100.01	2.24	138.7	7.6
	QCZ5-z4	1.1	26.0	589.4	316.7	0.6	663.8	362.7	0.67	101.08	2.34	150.4	8.3
	QCZ5-z5	1.1	30.0	911.4	504.0	0.6	1029.9	547.7	0.66	98.41	2.32	148.2	8.2
	Apatite												
	QCZ5-a1	2.8	42.5	14.9	74.9	5.2	32.5	4.0	0.69	22.81	0.42	33.2	1.8
	QCZ5-a2	2.5	39.0	9.6	48.2	5.2	20.9	2.4	0.67	21.24	0.4	31.8	1.7
	QCZ5-a3	2.1	42.5	11.1	58.1	5.4	24.6	3.1	0.67	22.93	0.39	34.1	1.8
	QCZ5-a4	2.0	41.5	8.2	42.2	5.3	18.1	1.8	0.67	18.54	0.39	27.8	1.5
Fangjiaweizi	QCZ6												
	Zircon												
	QCZ6-z1	2.7	28.0	333.1	78.4	0.2	351.5	145.0	0.76	76.54	1.48	100.3	5.4
	QCZ6-z2	1.4	30.0	270.5	70.5	0.3	287.1	154.4	0.69	99.62	2.21	144.2	7.9
	QCZ6-z3	4.5	38.0	152.9	27.1	0.2	159.3	114.0	0.79	132.1	2.63	166.4	9.0
	QCZ6-z4	6.5	45.5	716.3	225.8	0.3	769.4	246.4	0.81	59.5	1.72	73.2	4.2
	Apatite												
	QCZ6-a1[*]	1.3	34.0	3.9	11.4	3.0	6.6	3.2	0.62	89.45	4.18	144.3	9.9
	QCZ6-a2	1.1	34.0	4.0	8.9	2.3	6.1	1.0	0.62	29.89	0.99	48.6	2.9
	QCZ6-a4[*]	0.9	32.5	2.4	7.0	3.0	4.1	1.0	0.59	45.58	1.59	77.4	4.7
	QCZ6-a5[*]	1.2	34.5	5.1	13.1	2.7	8.1	3.3	0.62	73.86	3.42	119.3	8.1
	QCZ6-a7	0.7	28.5	5.6	7.7	1.4	7.4	0.9	0.56	22.63	0.9	40.1	2.6

Table 1 (*continued*)

	Sample	Mass (ug)	Radius[c] (um)	U (ppm)	Th (ppm)	Th/U	eU[a] (ppm)	He (nmol/g)	Ft[b]	Raw age (Ma)	± σ (Ma)	Cor age (Ma)	± σ (Ma)
Dadingzi	QCZ7												
	Zircon												
	QCZ7-z1	3.6	30.0	509.3	129.3	0.3	539.7	281.6	0.78	96.65	3.02	123.4	7.3
	QCZ7-z2	2.2	28.5	293.8	68.4	0.2	309.9	165.3	0.75	98.76	2.11	132.4	7.2
	QCZ7-z4[*]	9.8	41.5	88.2	30.1	0.4	95.3	41.3	0.84	80.47	1.83	95.6	5.3
	Apatite												
	QCZ7-a1	3.5	43.5	4.9	3.4	0.7	5.7	0.5	0.72	17.21	0.75	24.0	1.6
	QCZ7-a2	4.1	53.0	12.7	7.0	0.6	14.2	1.6	0.75	21.26	0.48	28.3	1.6
	QCZ7-a3[*]	2.5	41.0	5.5	4.3	0.8	6.5	1.1	0.70	30.62	0.74	44.0	1.7
	QCZ7-a4	1.6	38.5	7.7	6.3	0.8	9.2	1.1	0.66	22.16	0.63	33.5	1.3
	QCZ7-a5	1.5	36.5	7.6	5.8	0.8	8.9	0.7	0.65	14.88	0.44	22.9	1.3
	QCZ7-a6	1.4	37.5	4.5	11.1	2.5	7.1	0.6	0.64	14.65	0.74	22.8	1.6

eU[a]—effective U concentration that weighs U and Th for their alpha productivity and is computed as [u] + 0.235*[Th] (Flowers, 2009).

Ft[b]— alpha ejection correction (Farley et al., 1996).

Radius[c]— half the width of a single grain.

 * Single-grain ages have been rejected.

were collected from different locations throughout the Shuangdinggou plutons. Four zircon and six apatite grains from sample QCZ2 were analyzed, yielding ZHe ages that range from 107.0 ± 5.8 to 125.6 ± 7.7 Ma. An average value of 124.4 ± 1.8 Ma was calculated that excluded the younger zircon grain QCZ2-z5, and the AHe ages range from 28.5 ± 1.6 to 38.5 ± 2.0 Ma, with an average age of 32.3 ± 5.0 Ma. The zircon and apatite grains exhibit a narrow range of Th/U ratios. Five zircon and six apatite grains were analyzed from sample QCZ3. The five zircon grains yielded ages that range from 129.4 ± 7.2 to 142.6 ± 7.8 Ma (with an average age of 136.6 ± 5.6 Ma), and the six apatite grains yielded ages between 25.6 ± 1.4 and 35.6 ± 1.9 Ma (with an average age of 29.8 ± 3.8 Ma). We failed to obtain reliable (U-Th)/He ages for sample QCZ4, due to the extremely low helium contents in its zircon and apatite grains. The average values determined from the five ZHe ages and seven AHe ages of sample QCZ5 are 137.9 ± 15.4 Ma and 31.7 ± 2.8 Ma, respectively, and these values are similar to those of QCZ2 and QCZ3.

Sample QCZ6 was collected from the Fangjiaweizi granite, and the four analyzed zircon grains display a wide range of helium ages, of which the youngest is 73.2 ± 4.2 Ma, whereas the oldest is 166.4 ± 9.0 Ma (with an average age of 121.0 ± 42.1 Ma). Among the five apatite grains selected from sample QCZ6, three grains (QCZ6-a1, QCZ6-a4 and QCZ6-a5) got abnormally old ages, and the two remaining grains got ages of 48.6 ± 2.9 and 40.1 ± 2.6 Ma (with an average age of 44.4 ± 6.0 Ma).

Sample QCZ7 was obtained from the Proterozoic Dadingzi plagiogranite. Its three ZHe ages range from 95.6 ± 5.3 to 132.4 ± 7.2 Ma (with an average age of 127.9 ± 6.3 Ma, excluding zircon grain QCZ7-z4, which yielded a younger age), and its Th/U ratios range from 0.24 to 0.35. The five AHe ages range from 22.8 ± 1.3 to 33.5 ± 1.3 Ma, with an average age of 26.3 ± 4.6 Ma (excluding QCZ7-a3, which yielded an older age of 44.0 ± 1.7 Ma).

3.1.2.2. The Wulong orefield. Sample WL1 was collected from the Wulongbei porphyritic granite. The three zircon grains analyzed from this sample, WL1-z2, WL1-z3 and WL1-z4, yielded ages of 61.2 ± 3.3, 78.5 ± 4.3 and 114.8 ± 6.3 Ma, respectively. After excluding WL1-z4, which has an older age and a higher Th/U ratio than the other two zircon grains, we obtained an average ZHe age of 69.9 ± 12.3 Ma. The five analyzed apatite grains yielded ages ranging from 24.9 ± 0.9 to 36.2 ± 1.4 Ma, with an average age of 30.4 ± 5.3 Ma, and Th/U ratios ranging from 2.4 to 6.3. WL2 is also a granite sample that was collected from Wulongbei. Although one zircon grain (WL2-z1) yielded an anomalously young age, the other two grains got ages of 68.7 ± 3.8 and 42.0 ± 2.3 Ma, respectively, resulting in an average age of 55.35 ± 18.8 Ma. The four AHe ages obtained from sample WL2

range between 21.4 ± 1.2 and 31.5 ± 1.7 Ma, with an average age of 27.0 ± 4.1 Ma.

Samples WL3, WL4 and WL5 were collected from the Dingqishan porphyritic biotite granite. Although the zircon grains selected from WL4 contain too many inclusions and fractures for He analysis, samples WL3 and WL5 have similar ZHe average ages of 73.8 ± 4.0 Ma and 70.6 ± 3.5 Ma, respectively. Four apatite grains from WL3 yielded consistent ages ranging from 28.5 ± 1.6 to 32.8 ± 1.9 Ma and obtained a mean age of 31.1 ± 1.8 Ma, with Th/U ratios ranging between 6.7 and 8.6. Four apatite grains from WL4 yielded ages ranging from 25.8 ± 1.4 to 31.6 ± 1.8 Ma (with an average age of 28.9 ± 2.7 Ma) and Th/U ratios varying between 3.3 and 5.7. Since no eligible apatite grains were found in sample WL5, no AHe ages were obtained.

Samples WL6 and WL7 were collected from the Yanshanian Sanguliu granodiorite. The four ZHe ages obtained from WL6 range from 49.5 ± 3.9 to 61.3 ± 3.4 Ma (with an average age of 55.2 ± 4.9 Ma), and the three ZHe ages obtained from WL7 range from 43.0 ± 2.3 to 63.3 ± 3.5 Ma (with an average age of 62.3 ± 1.4 Ma, excluding the zircon grain WL7-z1, which got an age that is younger than the other two). The AHe ages from WL6 and WL7 are different. The four apatite grains collected from WL6 yielded consistent ages ranging from 31.6 ± 1.7 to 36.3 ± 1.9 Ma, with an average age of 33.6 ± 2.2 Ma, and relatively homogeneous Th/U ratios (3.2–3.9). The four apatite grains collected from WL7 display a wide range of ages ranging from 35.9 ± 2.0 to 56.7 ± 3.0 Ma (with an average age of 47.1 ± 8.7 Ma, which is much older than that of WL6).

Sample WL8 was collected from the Yanshanian gneissic granite. The four analyzed zircon crystals got ages between 66.1 ± 3.6 and 75.5 ± 4.1 Ma, with a mean age of 70.7 ± 4.5 Ma. The four AHe ages exhibit a scattered distribution ranging from 26.0 ± 1.6 to 51.1 ± 2.9 Ma, with an average age of 36.8 ± 11.5 Ma.

Previous research has shown that cooling rates usually correlate with (U-Th)/He ages. Slow cooling can result in samples remaining in the He partial retention zone (HePRZ) for long periods of time. Additionally, the concentration of U and Th is not only heterogeneous within individual grains but also varies from grain to grain. Some grains have cores with high concentrations of U and Th, whereas others have rims with high concentrations of U and Th. Slow cooling causes different degrees of diffusive loss of radiogenic ^{4}He from different grains to resulting in increasing discrepancies among single-grain ages. In contrast, rapid cooling limits the diffusion of ^{4}He and reduces the variation in single-grain ages (Fitzgerald et al., 2006). The analysis of the single-grain helium age distributions observed in the two orefields indicates that, although the partial ages display scatter, most of them are relatively consistent. Most of the ZHe ages obtained from the samples in the Qingchengzi orefield fall within the range of approximately 123–143 Ma (Fig. 4a), whereas most of the ZHe ages obtained

Table 2
Zircon and apatite (U-Th)/He ages for the samples from the Wulong orefield.

	Sample	Mass (ug)	Radius[c] (um)	U (ppm)	Th (ppm)	Th/U	eU[a] (ppm)	He (nmol/g)	Ft[b]	Raw age (Ma)	± σ (Ma)	Cor age (Ma)	± σ (Ma)
Wulongbei	WL1												
	Zircon												
	WL1-z2	2.1	34.0	1015.3	601.6	0.6	1156.7	276.7	0.73	44.5	0.9	61.2	3.3
	WL1-z3	2.5	30.0	606.0	477.5	0.8	718.2	227.6	0.75	58.8	1.3	78.5	4.3
	WL1-z4[*]	13.3	40.5	104.1	116.2	1.2	131.4	69.4	0.85	97.7	2.2	114.8	6.3
	Apatite												
	WL1-a1	2.4	43.0	15.3	52.0	3.5	27.5	2.6	0.69	17.1	0.3	24.9	1.3
	WL1-a3	3.4	47.5	8.2	28.2	3.5	14.9	2.1	0.72	26.0	0.5	36.2	1.9
	WL1-a4	1.4	34.0	11.0	44.8	4.2	21.6	1.9	0.62	16.5	0.4	26.7	1.5
	WL1-a5	1.9	39.0	11.3	26.4	2.4	17.5	2.3	0.67	23.9	0.5	35.9	1.9
	WL1-a6	1.5	36.0	3.7	22.7	6.3	9.0	0.9	0.63	17.6	0.5	28.1	1.6
	WL2												
	Zircon												
	WL2-z1[*]	4.2	35.5	498.8	356.4	0.7	582.5	24.5	0.79	7.8	0.1	9.9	0.5
	WL2-z3	11.6	43.0	163.5	151.7	1.0	199.1	62.5	0.85	58.2	1.5	68.7	3.8
	WL2-z4	3.2	31.0	538.3	393.8	0.8	630.9	109.9	0.77	32.4	0.7	42.0	2.3
	Apatite												
	WL2-a1	1.4	35.0	17.3	60.4	3.6	31.5	2.9	0.63	17.1	0.4	27.4	1.5
	WL2-a2	2.0	39.0	10.3	31.9	3.2	17.8	1.4	0.66	14.2	0.4	21.4	1.2
	WL2-a3	1.7	35.5	8.8	36.5	4.3	17.4	1.6	0.64	17.5	0.4	27.5	1.5
	WL2-a4	1.9	39.5	7.3	30.8	4.3	14.6	1.6	0.66	20.8	0.5	31.5	1.7
Dingqishan	WL3												
	Zircon												
	WL3-z1[*]	12.8	61.0	83.7	74.0	0.9	101.0	123.9	0.84	224.5	8.0	266.3	16.3
	WL3-z2[*]	9.3	39.0	464.2	384.3	0.9	554.5	56.2	0.84	18.9	0.4	22.6	1.2
	WL3-z3	7.3	36.5	215.7	179.8	0.9	258.0	84.6	0.82	60.8	1.2	73.8	4.0
	Apatite												
	WL3-a1	1.9	42.0	4.5	37.6	8.6	13.3	1.5	0.66	20.6	0.5	31.1	1.7
	WL3-a2	1.4	34.0	9.0	67.8	7.8	24.9	2.6	0.61	19.4	0.4	31.8	1.7
	WL3-a3	1.2	33.5	5.3	34.5	6.7	13.4	1.4	0.60	19.7	0.6	32.8	1.9
	WL3-a4	1.1	32.0	6.7	44.1	6.8	17.0	1.5	0.59	16.7	0.4	28.5	1.6
	WL4												
	Apatite												
	WL4-a1	1.4	34.5	4.7	26.0	5.7	10.8	1.1	0.62	19.5	0.5	31.6	1.8
	WL4-a2	2.0	40.5	22.2	71.6	3.3	39.0	3.6	0.67	17.3	0.4	25.8	1.4
	WL4-a3	1.1	32.5	11.8	45.6	4.0	22.6	71.0	0.60	18.4	0.5	30.8	1.8
	WL4-a4	1.3	32.5	25.5	94.2	3.8	47.6	4.3	0.61	16.8	0.4	27.5	5.4
	WL5												
	Zircon												
	WL5-z1	1.6	32.0	477.3	468.0	1.0	587.3	163.0	0.70	51.5	1.0	73.8	4.0
	WL5-z2	1.5	31.5	313.4	246.1	0.8	371.2	98.5	0.69	49.3	1.0	71.2	3.8
	WL5-z3[*]	2.4	31.0	353.1	323.3	0.9	429.1	151.7	0.74	65.6	1.2	88.1	4.7
	WL5-z4	1.2	30.5	410.8	435.4	1.1	513.1	124.1	0.67	44.9	0.9	66.8	3.6
Sanguliu	WL6												
	Zircon												
	WL6-z1	4.4	40.0	172.3	108.4	0.7	197.7	46.4	0.79	43.7	0.9	55.6	3.0
	WL6-z2	2.1	30.0	133.1	96.0	0.7	155.7	30.3	0.73	36.2	2.2	49.5	3.9
	WL6-z3	2.4	34.5	312.7	179.9	0.6	354.9	86.3	0.74	45.2	1.0	61.3	3.4
	WL6-z4	2.5	31.5	168.8	117.6	0.7	196.5	42.8	0.75	40.5	0.9	54.3	3.0
	Apatite												
	WL6-a1	2.0	37.0	13.9	46.6	3.4	24.9	2.8	0.65	21.0	0.4	32.1	1.7
	WL6-a2	2.5	44.5	15.4	58.1	3.9	29.1	4.0	0.69	25.2	0.5	36.3	1.9
	WL6-a3	1.5	37.5	20.0	62.8	3.2	34.8	4.2	0.64	22.1	0.5	34.4	1.9
	WL6-a4	1.3	33.5	19.8	76.7	4.0	37.8	4.0	0.62	19.4	0.4	31.6	1.7
	WL7												
	Zircon												
	WL7-z1[*]	1.4	31.5	572.8	581.2	1.0	709.3	112.3	0.68	29.4	0.6	43.0	2.3
	WL7-z3	2.3	41.5	953.9	251.4	0.3	1013.0	254.	0.74	46.7	1.0	63.4	3.5
	WL7-z4	2.4	31.5	446.4	288.3	0.7	514.1	126.1	0.74	45.6	1.0	61.3	3.3
	Apatite												
	WL7-a1	2.1	37.0	27.1	50.1	1.9	38.9	5.0	0.66	23.8	0.6	35.9	2.0
	WL7-a3	1.1	31.0	51.7	93.9	1.9	73.8	11.9	0.60	29.9	0.6	49.8	2.7
	WL7-a6	0.9	33.0	25.0	46.7	1.9	35.9	5.4	0.60	27.5	0.7	46.1	2.6
	WL7-a7	1.1	33.5	29.7	73.4	2.5	47.0	8.8	0.61	34.7	0.6	56.7	3.0

Table 2 (*continued*)

	Sample	Mass (ug)	Radius[c] (um)	U (ppm)	Th (ppm)	Th/U	eU[a] (ppm)	He (nmol/g)	Ft[b]	Raw age (Ma)	± σ (Ma)	Cor age (Ma)	± σ (Ma)
Migmatitic granite	WL8												
	Zircon												
	WL8-z1	5.4	42.0	234.3	34.5	0.2	242.4	78.9	0.80	60.5	1.2	75.5	4.1
	WL8-z2	4.6	31.5	76.8	33.1	0.4	84.6	26.7	0.80	58.6	1.1	73.5	3.9
	WL8-z3	3.1	41.0	126.9	93.9	0.8	149.0	40.1	0.76	49.9	1.0	66.1	3.6
	WL8-z4	4.5	38.0	371.4	70.4	0.2	387.9	112.3	0.79	53.8	1.2	67.9	3.7
	Apatite												
	WL8-a1	1.8	41.5	7.2	18.5	2.6	11.6	1.1	0.67	17.4	0.6	26.0	1.6
	WL8-a4	1.7	37.5	18.7	20.2	1.1	23.5	3.4	0.66	27.0	0.6	40.8	2.2
	WL8-a5	2.6	45.0	2.9	4.7	1.7	4.0	0.4	0.70	20.5	0.7	29.2	1.8
	WL8-a7	2.3	43.5	2.2	3.5	1.6	3.1	0.6	0.69	35.5	0.9	51.2	2.9

eU[a]—effective U concentration that weighs U and Th for their alpha productivity and is computed as [u] + 0.235*[Th] (Flowers, 2009).
Ft[b]— alpha ejection correction (Farley et al., 1996).
Radius[c]— half the width of a single grain.
* Single-grain ages have been rejected.

from the samples in the Wulong orefield fall within the range of 55 to 75 Ma (Fig. 4b). The AHe ages of the two orefields show distributions with similar ranges that are concentrated between 26 and 36 Ma (Fig. 4c and d). Therefore, the above data indicate that two pulses of rapid uplift likely occurred within the Qingchengzi orefield at 123–143 Ma and at 26–36 Ma, whereas two pulses of rapid uplift likely occurred in the Wulong orefield at 55–75 Ma and at 26–36 Ma. Moreover, the apatite ages from the Qingchengzi and Wulong orefields are obviously less scattered than the zircon ages, thus indicating that the apatites record a faster cooling.
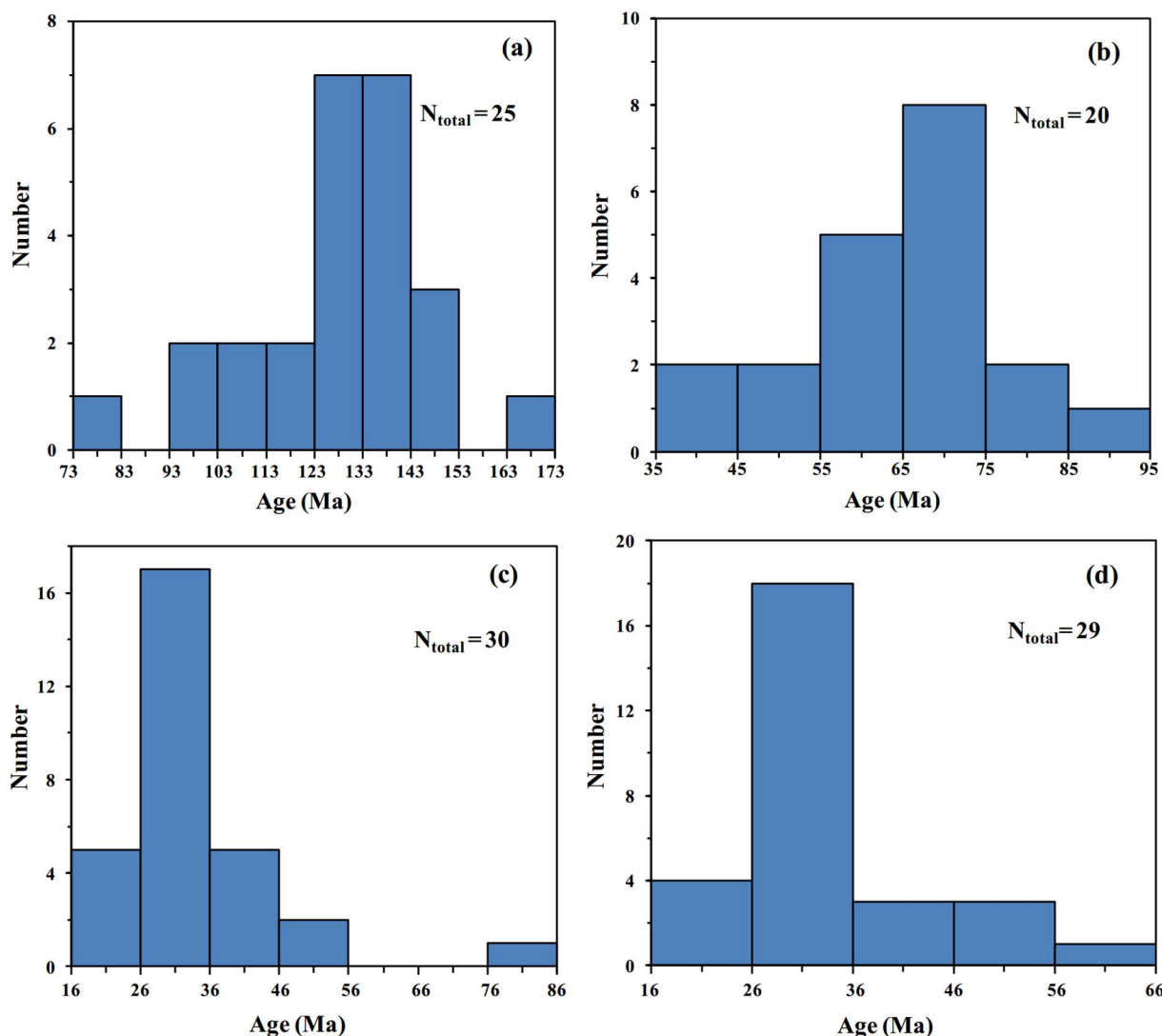
Fig. 4. Single-grain He age distributions. (a) Single-grain zircon (U-Th)/He age distribution of the Qingchengzi orefield. (b) Single-grain zircon (U-Th)/He age distribution of the Wulong orefield. (c) Single-grain apatite (U-Th)/He age distribution of the Qingchengzi orefield. (d) Single-grain apatite (U-Th)/He age distribution of the Wulong orefield. The ZHe ages of the two orefields are different whereas the AHe ages have similar distributions (N$_{total}$ represents the total number of grains).

Table 3

EPMA data of chemical composition (wt%) and calculated formula of hornblende from samples QCZ2, WL3 and WL6.

Sample	QCZ-2		WL-3		WL-6		
	D-1	D-2	D-1	D-2	D-1	D-2	D-3
Na_2O	1.34	1.44	1.58	1.57	1.44	1.35	1.50
SiO_2	45.50	46.54	45.50	45.78	45.55	46.15	45.87
Cr_2O_3	0.11	0.04	0.00	0.03	0.03	0.03	0.00
K_2O	0.84	0.63	0.92	0.87	0.86	0.89	0.88
MgO	9.59	13.90	9.55	9.66	10.57	10.65	11.70
MnO	0.52	0.24	0.91	0.93	0.64	0.62	0.44
CaO	11.30	11.05	11.47	11.35	11.69	11.53	11.44
Al_2O_3	7.25	7.92	7.98	7.92	8.44	8.02	8.16
FeO	20.21	14.23	19.56	19.48	18.06	18.19	16.02
TiO_2	0.90	2.12	1.12	1.24	1.32	1.15	1.75
NiO	0.00	0.05	0.00	0.00	0.01	0.02	0.00
Total	97.57	98.15	98.59	98.82	98.61	98.59	97.76
Structural formula calculated based on 23 oxygens							
Si	6.841	6.695	6.791	6.799	6.735	6.809	6.775
Al^{IV}	1.159	1.305	1.209	1.201	1.265	1.191	1.225
Al^{VI}	0.127	0.038	0.195	0.184	0.206	0.203	0.196
Ti	0.102	0.229	0.125	0.138	0.147	0.127	0.194
Cr	0.013	0.005	0.000	0.004	0.003	0.003	0.000
Fe^{3+}	0.622	0.880	0.464	0.509	0.481	0.532	0.424
Fe^{2+}	1.919	0.832	1.976	1.910	1.752	1.712	1.555
Mn	0.067	0.029	0.115	0.116	0.080	0.077	0.055
Mg	2.150	2.981	2.124	2.139	2.330	2.343	2.576
Ni	0.000	0.006	0.000	0.000	0.002	0.002	0.000
Ca	1.821	1.703	1.834	1.806	1.851	1.823	1.811
Na	0.390	0.402	0.457	0.452	0.413	0.385	0.430
K	0.161	0.116	0.174	0.165	0.161	0.167	0.166
Total	15.372	15.220	15.465	15.422	15.427	15.375	15.406

3.2. EPMA method

3.2.1. Analytical techniques

The chemical composition (in wt%) of hornblende was measured using the JEOL JXA-8100 of the EPMA and SEM Laboratory of the Institute of Geology and Geophysics, Chinese Academy of Sciences (IGGCAS). Unaltered and euhedral hornblende crystals selected from the thin sections of samples QCZ2, WL3 and WL6 were analyzed using electron microprobe analysis (EPMA). An acceleration voltage of 15 kV was applied with a current of 10 nA and a beam diameter of 5 μm.

3.2.2. Results

Based on the analytical results, the Al_2O_3 content of sample QCZ2 ranges from 7.25 to 7.92%; the Al_2O_3 content of sample WL3 ranges from 7.92 to 7.98%; and the Al_2O_3 content of sample WL6 ranges from 8.02 to 8.44% (Table 3). The contents of other bulk elements can be seen in Table 3. The calculated content of each cation is based on 23 oxygen atoms, and the results are shown in Table 3. The specific calculation method used here is described in detail by Schumacher (1997). For the three samples QCZ2, WL3 and WL6, the measured content of $Fe^{3+}/(Fe^{3+} + Fe^{2+})$ ranges from 0.2 to 0.5, and the content of $Fe_{total}/(Fe_{total} + Mg)$ ranges from 0.4 to 0.5; therefore, these data satisfy the conditions needed to use the Al-in-hornblende barometer suggested by Schmidt (1992) and Anderson and Smith (1995). The Al content used to estimate the emplacement depths of the plutons is the sum of Al^{IV} and Al^{VI}. Therefore, the total Al content in the hornblende from sample QCZ2 ranges between 1.286 and 1.343; the total Al content in the hornblende from sample WL3 ranges between 1.385 and 1.404; and the total Al content in the hornblende from sample WL6 ranges between 1.394 and 1.471 (Table 3).

4. Inverse modeling

After their formation, orebodies are frequently disturbed by various geologic events (Li et al., 2000, 2004; Guo et al., 2005; Wan et al., 2013). Regional uplift and denudation are the most important events

controlling the late-stage transformation and preservation of mineral deposits. In this section, we use the HeFTy software package (beta version 2; Ketcham, 2005) to simulate the low-temperature thermal histories of the Qingchengzi and Wulong orefields using the zircon and apatite (U-Th)/He thermochronology data. The ZHe and AHe ages of each sample are the averages of the single-grain ages, as described in Section 3.1.2. Because sample QCZ4 failed to yield reliable (U-Th)/He ages, sample WL4 yielded only an AHe age, and sample WL5 only yielded a ZHe age, these three samples are unsuitable for inverse modeling. Thus, the other twelve samples (QCZ1, QCZ2, QCZ3, QCZ5, QCZ6, QCZ7, WL1, WL2, WL3, WL6, WL7 and WL8) are utilized to simulate these cooling processes.

Several calibrations of the kinetic properties of apatite (Farley, 2000; Wolf et al., 1996), zircon (Reiners et al., 2004), and titanite (Reiners and Farley, 1999) have been published for use in HeFTy. When a given calibration model is chosen, several other parameters (i.e., the activation energy, geometry, and frequency factor of the target mineral) are automatically set to the corresponding default values. HeFTy also provides alternative methods for the correction of alpha stopping distances, including no correction, ejection and redistribution. For this alpha calculation, the second method is selected. For each sample, the starting time of the inverse modeling is set to the corresponding zircon (U-Th)/He age, and the apatite (U-Th)/He age is used as another time boundary condition. The temperature boundary conditions used in this study are the He closure temperatures of zircon and apatite, which are set to 180 °C and 65 °C, respectively. Prior to the inverse modeling, the specified constraints are shown as a series of boxes in the time-temperature window, similar to the gray squares shown in Fig. 5. The time-temperature histories are then forced to pass through these boxes. One constraint is always automatically defined at time = 0 (i.e., the present time). Based on the established parameter values, HeFTy then simulates 10,000 candidate evolutionary paths that can be expressed in three ways (as paths, path envelopes and constraint points), which are described in detail by Ketcham (2005). In this study, the simulation results are presented in the form of path envelopes (Fig. 5). In Fig. 5, the green region encompasses all acceptable paths, the magenta region encompasses all good paths, and the black solid line represents the best-fit evolutionary path. The details of the internal parameter sets used in all of the simulations are listed in Table 4.

4.1. Modeling results

The modeling results of the low-T thermal histories of the twelve samples collected from the two orefields are shown in Fig. 5. The crystallization pressures of samples QCZ2, WL3 and WL6, as calculated using the Al-in-hornblende barometer (Hammarstrom and Zen, 1986; Hollister et al., 1987; Johnson and Rutherford, 1989; Schmidt, 1992), are listed in Table 5. The average pressures of these three samples are 2.67 kbar, 3.06 kbar and 3.24 kbar, respectively. Assuming a lithostatic gradient of 3.5 km/kbar (based on a crustal density value of 2.80 g/cm^3; Cottle et al., 2007) in the studied region, these samples formed at depths of 9.3 km, 10.7 km, and 11.3 km, respectively. Based on a Mesozoic geothermal gradient of 42 °C/km, the temperatures at these depths could have reached 390–470 °C, which are all much greater than the (U-Th)/He closure temperature of zircon. Therefore, the cooling trajectory estimated using the (U-Th)/He method likely occurred due to structural uplift, rather than in situ magmatic cooling involving only the conduction and dissipation of heat. The six samples from the Qingchengzi orefield yielded different ZHe and AHe ages, but all of the simulations yielded similar cooling patterns that are characterized by transition from fast cooling to slow cooling, followed by another period of fast cooling and finally slow cooling (Fig. 5a–f). Moreover, the evolution of five of the samples (QCZ1, QCZ2, QCZ3, QCZ5 and QCZ7, but not QCZ6) demonstrated a high degree of consistency, based on their simulated good paths (i.e., magenta regions). The modeled cooling history of these five samples can clearly be divided into four stages
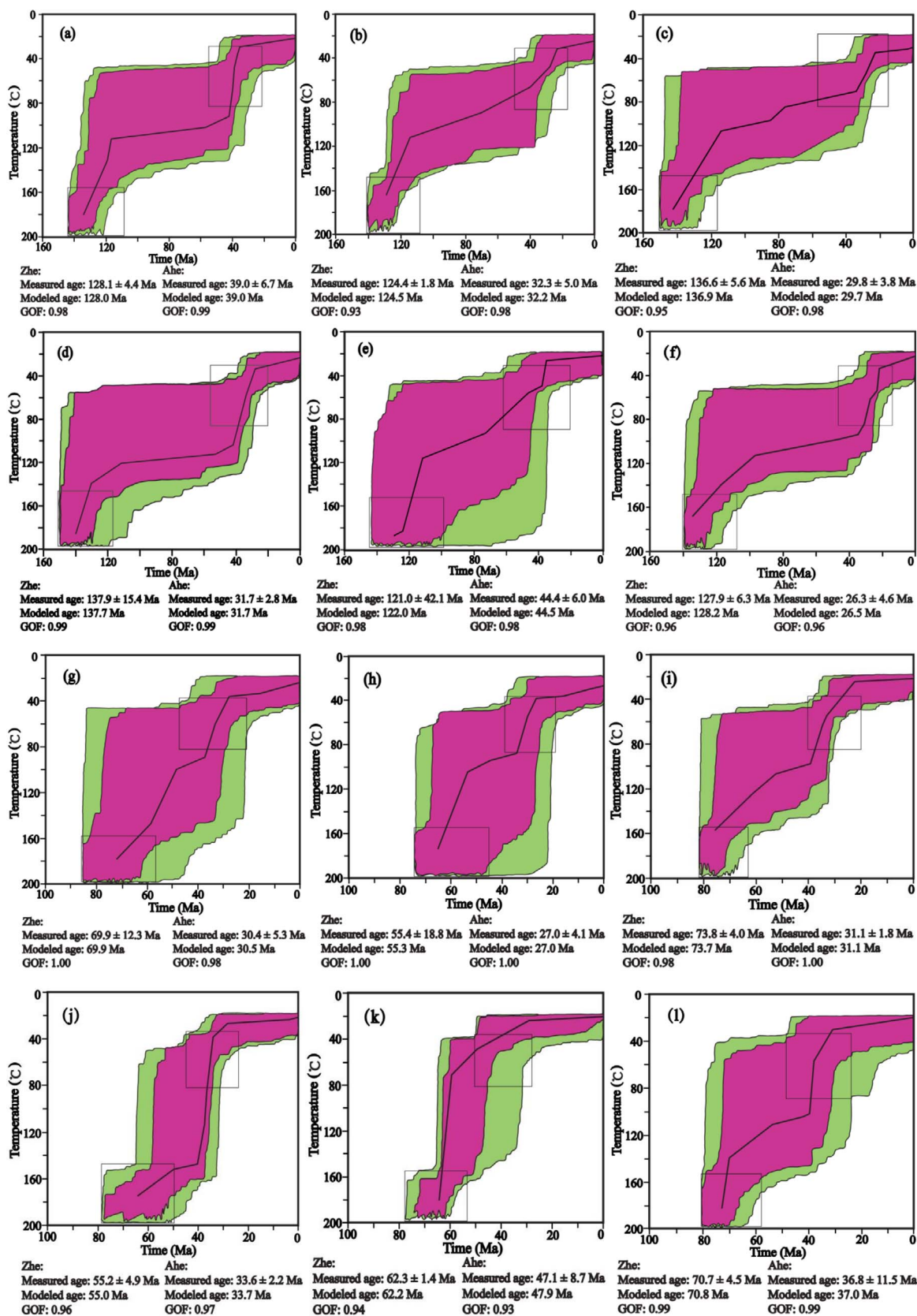
Fig. 5. The modeled thermal histories of samples QCZ1 (a), QCZ2 (b), QCZ3 (c), QCZ5 (d), QCZ6 (e) and QCZ7 (f) from the Qingchengzi orefield and samples WL1 (g), WL2 (h), WL3 (i), WL6 (j), WL7 (k) and WL8 (l) from the Wulong orefield obtained using the HeFTy software package. All helium ages used for inverse modeling are from this study. 0 Ma and 20 °C are the present time and the presumed surface temperature. The gray squares represent the temperature-time constraints imposed. The green region represents the acceptable evolutionary paths, the magenta region represents the better evolutionary paths, and the black curve represents the best-fit evolutionary path. Under each figure, the measured age, the age modeled using HeFTy and the goodness of fit (GOF) are displayed. The GOF is used to assess the fit between the modeled and measured ages, and values greater than 0.50 indicate "good" results.

Table 4
The parameters input into HeFTy, beta version 2.

Parameter	Option/value for zircon	Option/value for apatite
Calibration	Reiners et al. (2004)	Farley (2000)
Model precision	Best	Best
Activation energy	40.4 kcal/mol	32.9 kcal/mol
D_0	0.46 cm^2/N	50 cm^2/N
Alpha calculation	Ejection	Ejection
Age to report	Corrected	Corrected
Age alpha correction	Ketcham in prep.	Ketcham in prep.
Segment parameters	2G, gradual	2G, gradual

Table 5
The calculated crystallization pressures of QCZ2, WL3 and WL6 obtained using the Al-in-hornblende barometer.

Sample	QCZ-2		WL-3		WL-6		
	D-1	D-2	D-1	D-2	D-1	D-2	D-3
Al_{total}	1.286	1.343	1.404	1.385	1.471	1.394	1.421
Pressure (kbar)							
P1	2.55	2.83	3.14	3.05	3.48	3.09	3.23
P2	2.49	2.81	3.16	3.05	3.53	3.11	3.26
P3	1.98	2.22	2.48	2.40	2.76	2.44	2.55
P4	3.11	3.38	3.67	3.58	3.99	3.63	3.75
Average	2.53	2.81	3.11	3.02	3.44	3.07	3.20

P1, P2, P3 and P4 were calculated according to Hammarstrom and Zen (1986), Hollister et al. (1987), Johnson and Rutherford (1989) and Schmidt (1992), respectively.

(Fig. 5a–d, f): (1) moderately fast cooling during the Early Cretaceous (ca. 125 ± 10 Ma), when a 60–80 °C drop in temperature occurred over approximately 20 Ma at a cooling rate of 3–4 °C/Ma; (2) relatively slow cooling from the Late Cretaceous to the Early Eocene; (3) very fast cooling from the Late Eocene to the Oligocene (ca. 32 ± 6 Ma), with a 50–80 °C decrease in temperature occurring over approximately 10 Ma at a cooling rate of 5–8 °C/Ma; and (4) very slow cooling from the Oligocene to the present (ca. 25 Ma). These thermal histories indicate that the Qingchengzi orefield experienced a rapid denudation during the Early Cretaceous, followed by long-term but weak erosion from the Late Cretaceous to the Early Eocene. Subsequently, increased denudation occurred from the Late Eocene to the Oligocene, indicating that the tectonic uplift in this period was stronger than that in the first stage. Finally, the Qingchengzi orefield entered a period of tectonic quiescence ca. 25 Ma. The best-fit path of sample QCZ6 is distinctly different from those of the other five samples and is characterized by a relatively rapid cooling from 130 to 38 Ma and by a quiescent stage starting at 38 Ma. However, this path still exhibits the two episodes of intensive cooling that occurred in the Early Cretaceous and in the Late Eocene to the Oligocene.

In contrast, the modeling results of the six samples obtained from the Wulong orefield appear to be slightly more complex. Samples WL1, WL2, WL3 and WL8 exhibit similar cooling patterns (Fig. 5 g–i, l), whereas samples WL6 and WL7 exhibit significantly different paths (Fig. 5j, k). Based on the evolutionary paths of samples WL1, WL2, WL3 and WL8, the cooling history of the Wulong orefield can be divided into four periods: (1) relatively fast cooling from the end of the Late Cretaceous to the Early Eocene (ca. 60 ± 10 Ma) with a cooling rate of 3–5 °C/Ma; (2) relatively slow cooling from the Early Eocene to the Late Eocene (ca. 50–39 Ma); (3) very fast cooling from the Late Eocene to the Oligocene, with a decrease in temperature from 110 to 100 °C to 40–30 °C occurring over approximately 10 Ma at a cooling rate of 6–8 °C/Ma (this cooling is consistent with the characteristics of stage three in the Qingchengzi orefield); and (4) slow cooling since the Oligocene.

Although WL6 and WL7 were collected from the same intrusion (i.e., the Sanguliu granodiorite), their simulated paths are very different. From the end of the Late Cretaceous to the Early Eocene, the simulated results of sample WL6 are characterized by relatively gradual change, while those of sample WL7 are characterized by a steep trajectory. From the Late Eocene to the Oligocene, the simulated results obtained with both samples record opposite situations (Fig. 5j, k). These two samples, which were collected within 2–3 km of each other from the same intrusion, yielded different results that generally do not conform to the common geologic evolution of the region. Therefore, the modeling results of samples WL1, WL2, WL3 and WL8 are believed to reflect the thermal history of the Wulong orefield.

The tectonic evolution of the Wulong orefield is similar to that of the Qingchengzi orefield, which also experienced periods of accelerated uplift and denudation, followed by subsequent periods of quiescence. However, the magmatic activity in the Wulong orefield occurred later than that in the Qingchengzi orefield, which may reflect differences in the tectonic settings of these two orefields during the Cenozoic. A relatively intense tectonic event occurred from the end of the Late Cretaceous to the Early Eocene, which resulted in the rapid cooling of the Wulong orefield. A period of very slow cooling then took place between 50 and 39 Ma. The rapid cooling that is inferred to have occurred afterward, from the Late Eocene to the Oligocene, was likely associated with a period of rapid denudation, thus implying tectonic reactivation. Finally, very slow cooling occurred after the Oligocene. This slow cooling makes up the final stage of this cooling history and likely reflects an episode of tectonic stabilization. The modeling results of the Qingchengzi and Wulong orefields are consistent with direct observations from the age distributions of zircon and apatite (Section 3.1.2, Fig. 4), although the cooling process determined based on the age distributions is slightly different from that simulated by HeFTy.

To sum up, we conclude that: 1) the cooling events occurred during the evolution histories of both orefields were episodic; 2) the Qingchengzi orefield was subject to the uplift during the Early Cretaceous and from the Late Eocene to the Oligocene, whereas the Wulong orefield experienced the uplift from the end of the Late Cretaceous to the Early Eocene and from the Late Eocene to the Oligocene; and 3) the cooling from the Late Eocene to the Oligocene was comparatively extensive and rapid.

5. Discussion

5.1. Reasons for age dispersion

Most of the samples discussed in this study record dispersion in single-grain ages that far exceeded the analytical error (Tables 1 and 2), especially in the ZHe ages. In general, the possible reasons for this variation include helium contributions from indiscernible U/Th-rich inclusions (Fitzgerald et al., 2006), ^{4}He implantation from the surrounding matrix (Spencer et al., 2004; Spiegel et al., 2009), the effect of different particle sizes (Farley, 2000; Reiners and Farley, 2001), contributions of radiogenic ^{4}He from the decay of ^{147}Sm (Reiner and Nicolescu, 2006), the alpha particle injection effect (Farley et al., 1996; Fitzgerald et al., 2006) and radiation damage (Shuster et al., 2006; Flowers, 2009).

The presence of U- and Th-rich solid inclusions in the grains could have a strong impact on the ages, especially for apatite. The most common U/Th-rich inclusions in apatite are zircon and monazite, which are insoluble in the nitric acid used to dissolve apatite. Therefore, these phases do not contribute U and Th, but they do contribute ^{4}He during the extraction of gas by laser heating, leading to erroneously old ages.

In contrast, the ZHe ages are less affected by the presence of solid inclusions because the zircon grains are highly enriched in U and Th and dissolve completely during the hydrofluoric acid procedure. In addition, fluid inclusions are also an important source of radiogenic ^{4}He and are generally considered to provide "excess He" (Ballentine et al., 2002). Thus, fluid inclusions are often regarded as a reason for abnormal ages (Stockli et al., 2000). Besides, the presence of U/Th-rich
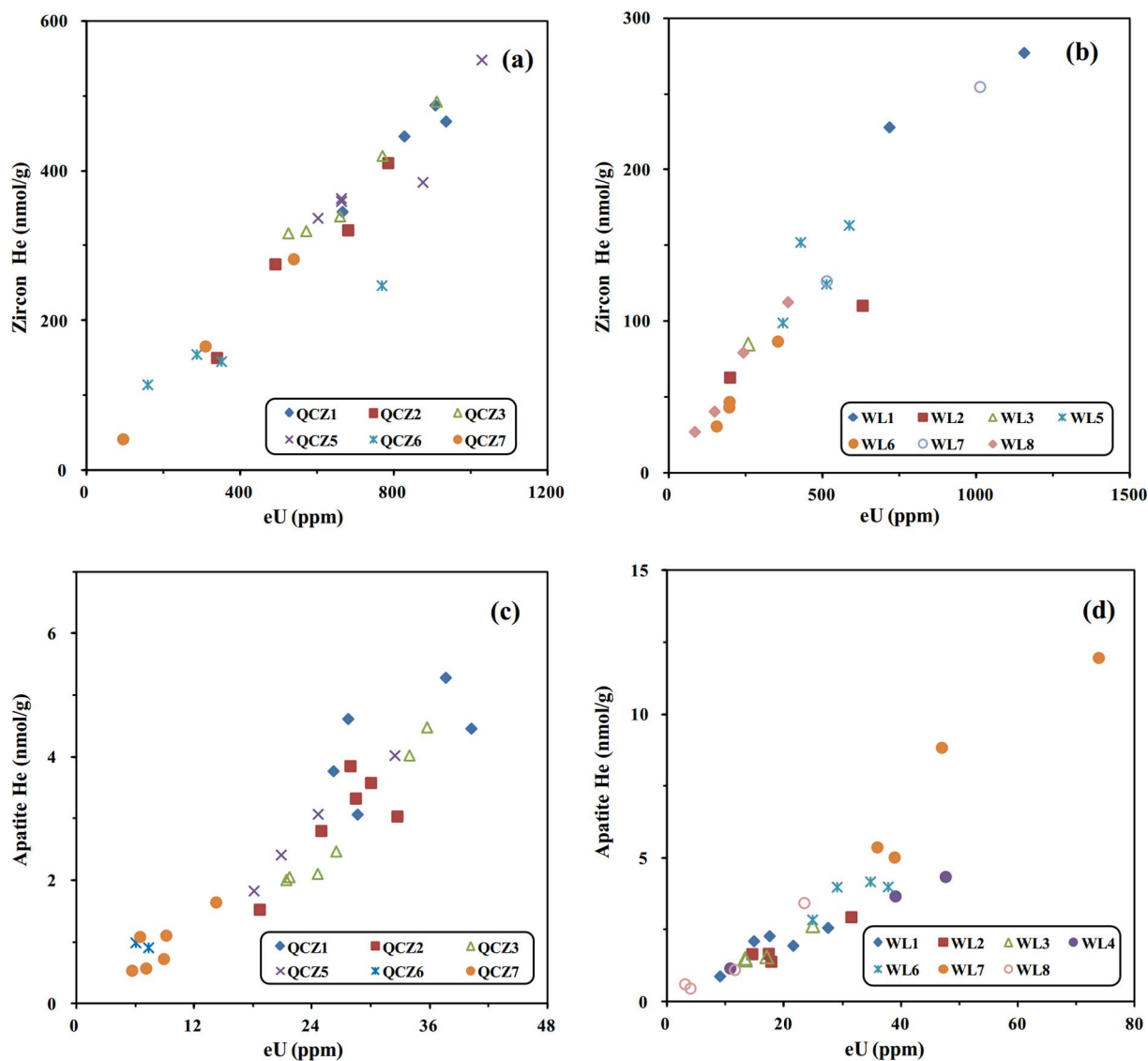
Fig. 6. Relationship between the effective U concentration (eU) and He concentrations. (a) Zircon He concentrations versus eU of the Qingchengzi orefield. (b) Zircon He concentration versus eU of the Wulong orefield. (c) Apatite He concentration versus eU of the Qingchengzi orefield. (d) Apatite He concentration versus eU of the Wulong orefield. In the four graphs, eU is positively correlated with the He concentrations, and the existence of "excess He" can be ruled out.

mineral phases within zircon and apatite grains is likely to implant excess He into these crystals (Spiegel et al., 2009). However, the positive linear correlations between the effective uranium concentration eU, which weights U and Th for their alpha productivity and is calculated as [U] + 0.235*[Th], and the He concentrations of zircon and apatite (Fig. 6) indicate that there is no obvious excess ^{4}He within the analyzed crystals. Therefore, the effects of inclusions and external He on the ages can be excluded.

Some studies have shown that the grain sizes of zircon and apatite may affect their effective diffusion domains and helium closure temperatures. Relatively large grains usually yield older ages, due to their larger diffusion domains, which have higher closure temperatures (Farley, 2000; Reiners and Farley, 2001). Nevertheless, most of the grains from the Qingchengzi and Wulong orefields do not exhibit clear correlations between ages and grain sizes (Fig. 7). Thus, no correlation exists between grain sizes and ages, implying that grain sizes rarely affect the ages.

Due to the relatively long half-life of ^{147}Sm and the small amount of daughter products that it yields, the alpha decay of ^{147}Sm is considered to have a negligible effect on (U–Th)/He ages. Reiners and Nicolescu (2006) indicated that ^{147}Sm contributes approximately 5% of

radiogenic ^{4}He only when U concentrations are less than 5 ppm. Tables 1 and 2 show that most of the apatite grains examined in this study display U concentrations that are higher than 5 ppm, whereas the zircon grains display much higher U concentrations that reach up to hundreds of parts per million. Therefore, the ^{4}He derived from ^{147}Sm accounts for a very small proportion of the total ^{4}He and has little impact on intra-sample age variations.

Alpha particles (^{4}He) produced during the decay of U and Th have a high initial kinetic energy of approximately 8 MeV, which can cause them to move between 11 and 34 μm before stopping. This distance is defined as the alpha particle stopping distance. As a result, alpha particles produced near the edges of grains can easily escape from the grains, resulting in the loss of ^{4}He and underestimated ages. Therefore, to obtain a relatively true age, the raw data must be corrected (F_T correction) (Farley et al., 1996). This correction is based on two key assumptions: (1) alpha particles implanted into crystals from the surrounding matrix can be ignored, and only alpha ejection must be considered (as seen in Fig. 6, the alpha particles implanted from outside of the crystal are insignificant), and (2) the uniform distribution of U and Th within the grains is generally postulated. However, in practice, the distribution of U and Th is heterogeneous within individual grains and
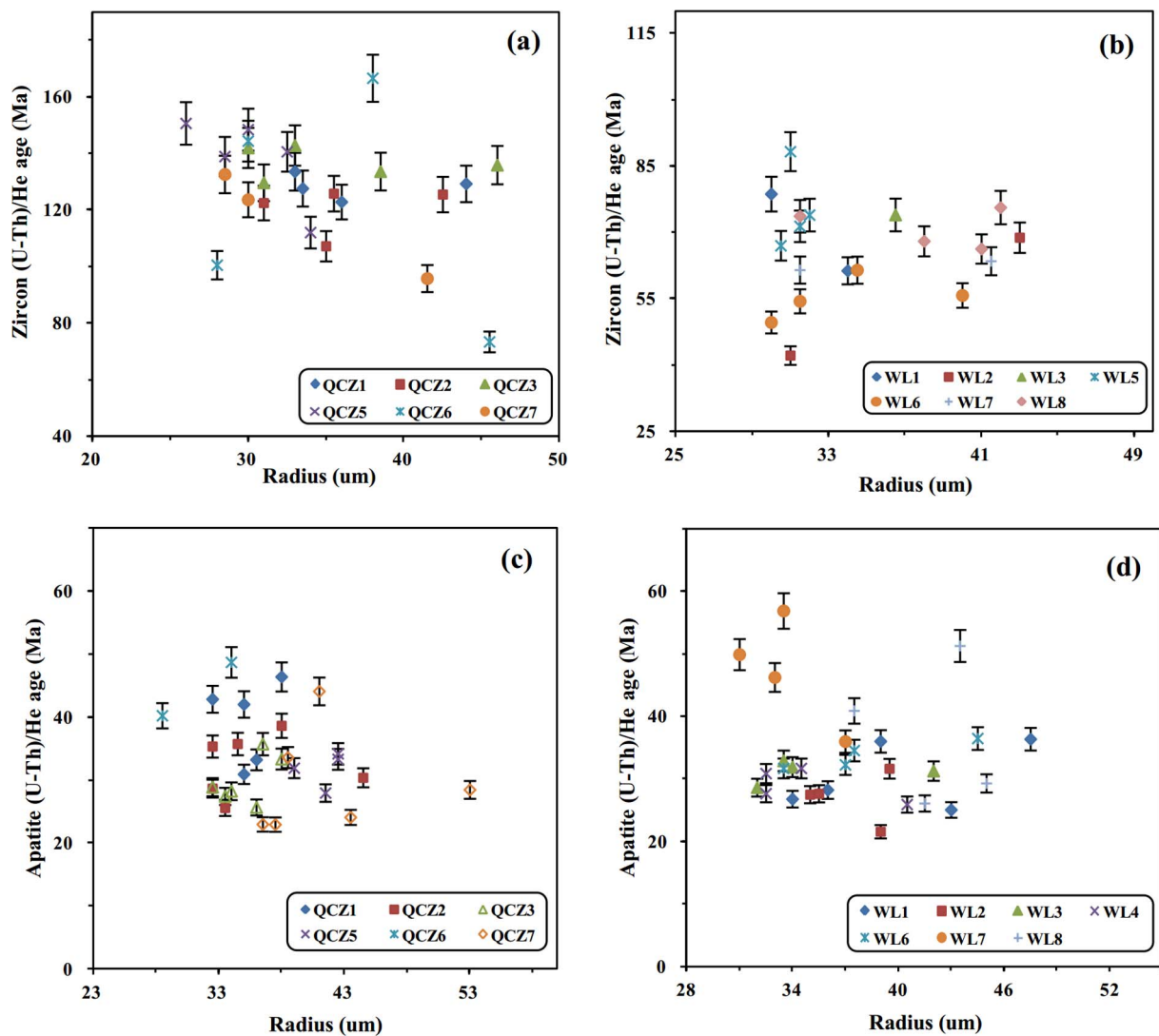
Fig. 7. Relationship between grain radius and age. (a) The ZHe ages versus the grain radius (half the width of a single grain) values of the Qingchengzi orefield. (b) The ZHe ages versus the grain radius values of the Wulong orefield. (c) The AHe ages versus the grain radius values of the Qingchengzi orefield. (d) The AHe ages versus the grain radius values of the Wulong orefield. No correlation between zircon and apatite He ages and radius was found.

varies between grains. Some grains have cores with high concentrations of U and Th, whereas others have rims with high concentrations of U and Th. If the same correction is applied to both types of grains, the former will yield older ages, and the latter will yield younger ages (Fitzgerald et al., 2006). In this case, the F_T correction will produce dispersed ages, even if the grains are from the same sample.

Radiation damage refers to the small, isolated spaces created during the radioactive decay of U and Th and can be expressed quantitatively using eU. Recent studies have demonstrated that the accumulation of radiation damage is generally conducive to trapping He in damaged spaces and hinders the diffusive loss of He (Farley, 2000; Flowers, 2009; Shuster et al., 2006). However, when radiation produces enough damages making the spaces link together to form a network, the diffusion of helium is promoted (Shuster et al., 2006). The ZHe and AHe ages of most of the samples from the Qingchengzi orefield are positively correlated with eU (Fig. 8a, b), except sample QCZ6 shows a negative correlation (Fig. 8a, b). In contrast, both negative and positive correlations between ZHe and AHe ages and eU are exhibited in the samples collected from the Wulong orefield, as shown in Fig. 8c and d. In addition, correlations between age and eU cannot be recognized in some samples, such as WL4 (Fig. 8d). These results suggest that radiation damage plays an important role for the wide range of ages, although the

influencing mechanism requires further analyses.

Based on the above discussion, we can exclude the effects of inclusions, the implantation of extraneous ^{4}He, contributions from ^{147}Sm and grain size. Instead, the ejection of alpha particles and radiation damage exert crucial impacts on the ages.

5.2. The exhumation and cooling rates and estimates of erosion in the Liaodong Peninsula

Average exhumation rates can generally be calculated using the age-closure temperature method, the mineral-pair method, or the age-elevation relationship method (Ding et al., 2007; Chang and Zhou, 2010). The last approach is appropriate for samples collected from a vertical section. Because all of the samples in this study were collected from surface outcrops, the first two approaches were chosen. The average cooling rate is equal to the ratio of the exhumation rate to the geothermal gradient. The depth of erosion can be expressed as the product of the exhumation rate and the corresponding cooling time. The cooling ages, the helium closure temperature, the geothermal gradient and the surface temperature represent crucial information that is used in this calculation.

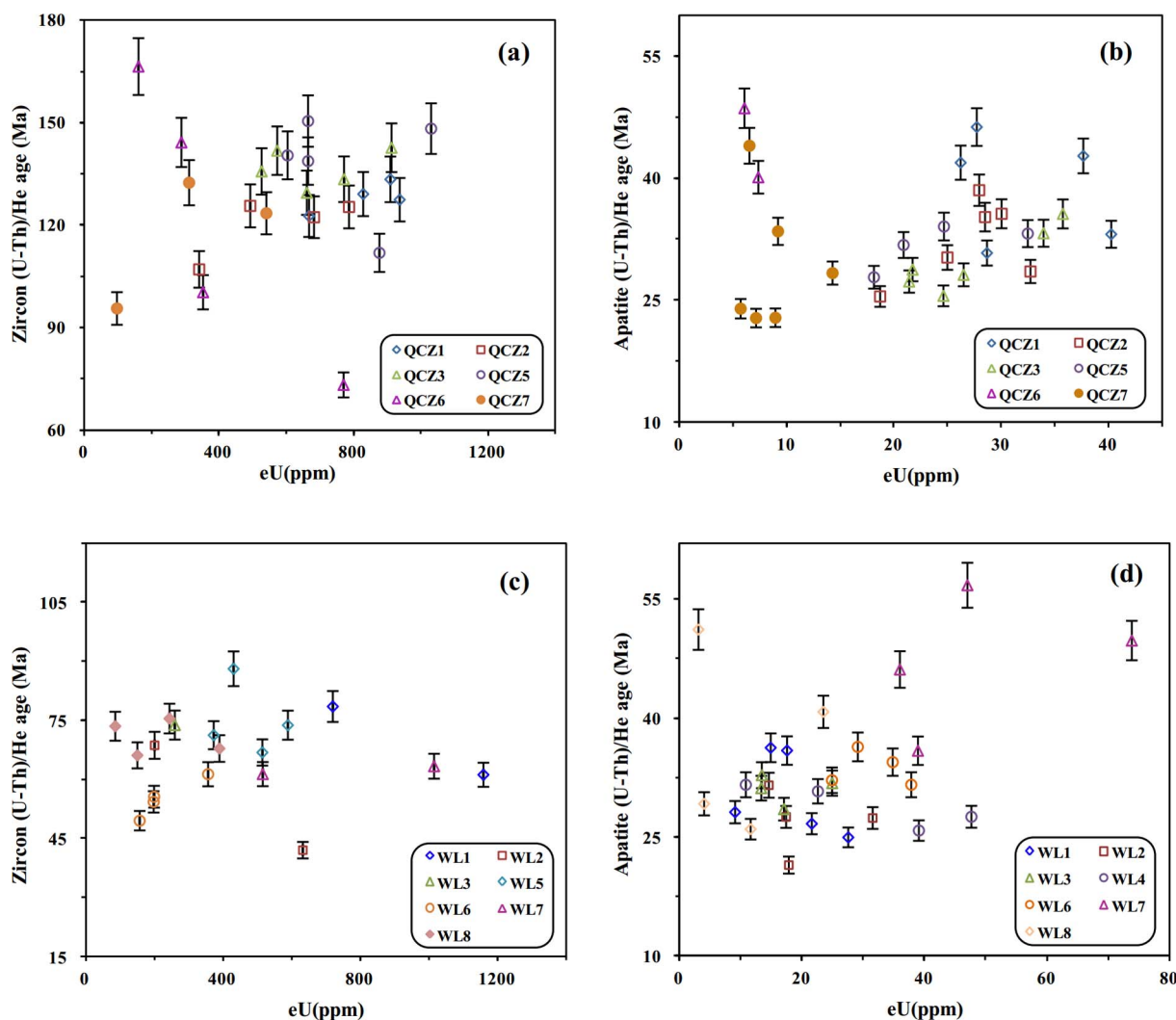According to the similarity of the modeling results obtained for

Fig. 8. Relationship between eU values and ages. (a) and (b) The ZHe ages and AHe ages versus the eU values of the Qingchengzi orefield. The ages and eU values are mostly positively correlated. (c) and (d) The ZHe ages and AHe ages versus the eU values of the Wulong orefield. Most of the samples show both positive and negative correlation between the ages and the eU values.

different samples collected from the same orefield (in Section 4.1), the mean ages were used here, i.e., we average the ages of all of the samples distributed within the same orefield to represent the (U-Th)/He ages of the orefields. The ZHe and AHe ages of the Qingchengzi orefield are 129.3 ± 6.7 Ma and 33.9 ± 6.6 Ma, respectively, and the ZHe and AHe ages of the Wulong orefield are 65.4 ± 7.8 Ma and 33.5 ± 6.8 Ma, respectively. The He closure temperatures of zircon and apatite are set to 180 °C and 65 °C, respectively. The geothermal gradient is estimated to have been approximately 30 °C/km since the Late Eocene, 37 °C/km from the Paleocene to the Early Eocene and 42 °C/km during the Mesozoic (He et al., 1995; Ren et al., 2001; Li et al., 2001; Lv, 2006). The mean surface temperature is assumed to be 15 °C.

With the above closure temperatures, geothermal gradients and surface temperature, the exhumation and cooling rates and eroded thicknesses of both orefields can be estimated. From 129 to 33 Ma, the average exhumation and cooling rates of the Qingchengzi orefield were 28.7 m/Ma and 1.21 °C/Ma, respectively, and the denudation was 2.7 km. After 33 Ma, these values shifted to 49.2 m/Ma, 1.47 °C/Ma and 1.6 km, respectively. The total eroded depth since 129 Ma is approximately 4.3 km. Compared with the Qingchengzi orefield, the Wulong orefield experienced more intense adjustments, with an exhumation rate of 97.4 m/Ma, a cooling rate of 3.61 °C/Ma and an eroded thickness of 3.1 km from 65 to 33 Ma. After 33 Ma, these values became

49.7 m/Ma, 1.49 °C/Ma and 1.6 km, respectively. A total of 4.7 km of crustal material has been eroded since 65 Ma. The erosion of the Wulong orefield, which is located in the eastern portion of the Liaodong Peninsula, is greater than that of the Qingchengzi orefield, which is located to the west. Therefore, we imply that the eastern part of the Liaodong Peninsula is deeper eroded than the western part.

The ore-forming pressure can be obtained by the following empirical formula (Shao, 1988):

$$P = (219 + 26.20*S)*T/(314 + 9.20*S) \tag{1}$$

where S and T is the salinity and homogenization temperature of fluid inclusions, respectively.

Using the previous salinity and homogenization temperature data of fluid inclusions in the quartz veins of the Qingchengzi and Wulong orefields at the metallogenic stage (Wang et al., 2010a; Wang et al., 2010b; Yang et al., 2016), we conclude that the ore-forming pressures of the Pb-Zn and Au-Ag deposits in the Qingchengzi orefield are 15.1–32.2 MPa and 10.1–21.9 MPa, respectively, whereas the ore-forming pressure of the Wulong gold deposit is 21.2–31.0 MPa. Because the mineralization pressures of the two orefields are both less than 40 MPa, the ore-forming depth can be estimated using the following equation, which is a function of the ore-forming pressure: H = P/10 (P = < 40 MPa), where H is the ore-forming depth, P is the metallogenic pressure, and the value 10 represents the hydrostatic pressure

gradient determined by Sun et al. (2000).

The ore-forming depths of the Qingchengzi Pb-Zn and the Au-Ag deposits are estimated to be 1.5–3.2 km and 1.0–2.2 km, respectively, whereas the ore-forming depth of the Wulong gold deposit is estimated to be approximately 2.1–3.1 km. The mineralization depth of the Qingchengzi Pb-Zn deposits is a bit deeper than that of the Au-Ag deposits.

Based on the comparison of ore-forming depth and the estimated denudation of the Qingchengzi orefield (ca. 4.3 km), the Pb-Zn and Au-Ag orebodies underwent different degrees of denudation, i.e., approximately 1.1–2.8 km and 2.1–3.3 km, respectively. Similarly, the mineralization depth of the Wulong gold deposit is also less than its eroded thickness (ca. 4.7 km), which implies that the gold orebodies were eroded approximately 1.6–2.6 km. In contrast, the metallogenic depth of the gold deposits in the Jiaodong Peninsula mainly ranges between 2.5 and 12.7 km (Lv et al., 2000; Chen, 2001; Zhou et al., 2008; Li et al., 2009; Guo et al., 2011), and the corresponding denudation ranges between 2.0 and 4.2 km (Liu et al., 2010; Chen, 2013). Under these conditions, the orebodies are well preserved. Consequently, the orebodies located in the Liaodong Peninsula were heavily transformed and eroded by later geologic events.

5.3. Implications for orefield evolution in northeast China

Our study of the orefields in the Liaodong Peninsula may shed light on the evolution of orefields in northeast China. To the southwest of the Liaodong Peninsula is the Jiaodong Peninsula, which is separated from the Liaodong Peninsula by the Bohai Bay (Fig. 1). The two adjacent areas in northeast China not only contain very important metallogenic orefields but also have generally similar geologic settings.

The Jiaodong Peninsula is another important metallogenic area in northeast China. This area features more than 200 Au mines, including the world-class Linglong, Sanshandao, Xincheng and Jiaojia Au deposits. To date, the combined use of different dating methods has indicated that the deposition of Au in the Jiaodong Peninsula occurred primarily during the Early Cretaceous (Zhang et al., 2003; Chen et al., 2004; Li et al., 2003, 2006; Hu et al., 2004, 2013; Fan et al., 2016). The development of the mineral deposits in the Liaodong Peninsula is complex and their precise age of mineralization has not yet been determined; however, previous studies indicate that it occurred roughly between the Triassic and Early Cretaceous (Wei et al., 2001, 2003, 2004; Liu and Ai, 2002; Xue et al., 2003; Yu et al., 2009). Therefore, the thermal evolution that occurred after the Early Cretaceous played a key role in the transformation and preservation of the orebodies in the Jiaodong and Liaodong peninsulas.

In Section 4.1, we simulated the thermal histories of the orefields in Liaodong Peninsula. The results imply that the Qingchengzi orefield experienced the uplift during the Early Cretaceous and during the Late Eocene to the Oligocene, whereas the Wulong orefield was uplifted toward the near-surface during the end of the Late Cretaceous to the Early Eocene and during the Late Eocene to the Oligocene. These two orefields underwent multiple periods of cooling and experienced the same rapid cooling at approximately 30 ± 5 Ma. The main metallogenic epoch of the deposits in the Qingchengzi orefield (ca. 220–130 Ma; Liu and Ai, 2002; Xue et al., 2003; Yu et al., 2009) occurred much earlier than that of the Wulong gold deposit (ca. 112 Ma; Wei et al., 2004). Therefore, the Early Cretaceous rapid cooling (125 ± 10 Ma) recorded by the intrusions in the Qingchengzi orefield scarcely affected the Wulong orefield. Whereas, the rapid cooling that took place from the end of the Late Cretaceous to the Early Eocene, as recorded by the intrusions in the Wulong orefield, is not reflected in the thermal history of the Qingchengzi orefield. Two possible reasons for this phenomenon are that 1) the area affected by this cooling event was small and limited to the region around the Wulong orefield, or 2) the cooling event also affected the Qingchengzi orefield but was not recorded there. Determining which of these explanations is correct

requires further research on the regional tectonic setting.

Some scholars have used fission track and (U-Th)/He methods to detailedly study the thermal histories of the orebodies in the Jiaodong Peninsula. Samples collected from the Xincheng deposit were analyzed using apatite fission track (AFT) dating, and the results indicated that a rapid cooling event occurred at ca. 75–50 Ma (Deng et al., 2015). In addition, zircon and apatite (U-Th)/He analyses were conducted on samples collected from a borehole in the Jiaojia orefield, and the thermal histories were modeled using HeFTy. The results implied that two stages of rapid cooling occurred during 120–110 Ma and 75–60 Ma (Sun et al., 2016). Moreover, the AFT method was also used to reveal that the Sanshandao gold deposit also experienced relatively rapid cooling with a rate of 3.3 °C/Ma at ca. 60 ± 10 Ma (Zhang et al., 2016).

In addition to studies of the thermal evolution of large goldfields located in northwestern Jiaodong, the granitoid rocks distributed in the eastern region of the Jiaodong Peninsula have also been used to reconstruct the thermal history of the region. The Sanfoshan intrusion, located in the eastern Jiaodong, is an Early Cretaceous granite. The peak AFT age was approximately 33 Ma, which represents a rapid cooling of the Sanfoshan intrusion during the Early Tertiary (Zhao, 2015).

In summary, the cooling histories of these orefields and intrusions in the Jiaodong Peninsula are largely consistent with those of the orefields in the Liaodong Peninsula, i.e., rapid cooling occurred during the Early Cretaceous, the end of the Late Cretaceous-the Early Eocene and the Late Eocene-Oligocene, although the time span of these cooling events differ slightly. The three stages of relatively rapid cooling contribute to revealing the transformation and preservation situation of the deposits on the two peninsulas.

The Tan-Lu and Yalujiang fault zones, two large-scale regional geology structures, are considered to be of key significance to the tectonic evolution of orefields in northeast China. The Tan-Lu fault zone suffered polychronous and diverse evolutions in the Mesozoic and Cenozoic era. It is widely accepted that the Tan-Lu fault zone experienced sinistral movement during the Early Cretaceous (Wang et al., 2006; Zhang and Dong, 2008; Zhu et al., 2016). However, various researchers held different views on its evolutionary features after the Early Cretaceous. Zhu et al. (2004) reported that the Tan-Lu fault zone turned into a huge extensional structure during the Late Cretaceous to the Early Tertiary, then followed by a Late Tertiary compressive activity. Sun et al. (2010) revealed that right-lateral compression shearing from the end of Late Cretaceous to the Paleocene and right-lateral strike-slip from the Paleocene to the Eocene occurred along the Tan-Lu fault zone, which was subsequently deformed by compressional thrust movement during the Oligocene. Huang et al. (2015) presented that the Cenozoic evolutionary histories of the Tan-Lu fault zone began with extensional deformation before 40 Ma, and a dextral shearing took place from 40 to 25 Ma due to the subduction of the Pacific Plate. In addition, many other researchers also attempted to explain the evolution of the Tan-Lu fault zone (Grimmer et al., 2002; Zhang et al., 2003, 2015). Considered together with the thermal evolution of the orefields in the Liaodong and Jiaodong Peninsulas, we suggest that sinistral movement during Early Cretaceous, right-lateral compression shearing from the end of Late Cretaceous to the Paleocene and compressional thrust or dextral shearing movement at about Oligocene probably triggered the basically consistent uplift and erosion of the orefields in the Liaodong and Jiaodong Peninsulas.

The Yalujiang fault zone, a secondary fault zone of the Tan-Lu fault system, also reveals multiple deformational phases since the Triassic. According to the previous studies (Dong et al., 1989; Zhang et al., 2006), the tectonic evolution of the Yalujiang fault zone was divided into four stages. In the Late Triassic – Early Jurassic, sinistral strike-slip ductile shearing activity occurred. Afterwards, a low-angle extensional slip took place from the Middle to Late Jurassic. From the Early Cretaceous to the Late Cretaceous occurred the left-lateral normal strike-

slip movement, which was the main deformation of the fault. Subsequently, a right – lateral strike-slip movement along the Yalujiang fault continued through the end of the Late Cretaceous and Neogene. Based on the time range of the faulting, the latter two stages, from the Early Cretaceous to Late Cretaceous and from the end of the Late Cretaceous to Neogene, played important roles in accelerating the uplift and erosion of the orefields in the Liaodong Peninsula.

However, there are several different views on the uplift and cooling of the Jiaodong Peninsula. For example, zircon fission track ages from the Sanfoshan intrusion yielded a peak age of approximately 96 Ma, indicating that a cooling event occurred in the late Early Cretaceous (Zhao, 2015). Moreover, Sun et al. (2016) also reported that a short, rapid exhumation event occurred in the Jiaodong area at ca. 100–95 Ma. This cooling episode has not yet been identified in the thermal histories of the orefields in the Liaodong Peninsula. It may be due to lacking of multi-method thermochronology researches on the Liaodong Peninsula. Besides, further studies are needed to explore the tectonic mechanism responsible for the uplift of orebodies.

6. Conclusions

In this study, zircon and apatite (U-Th)/He ages have been obtained from the Shuangdinggou, Xinling, Dadingzi, Fangjiaweizi, Sanguliu, Wulongbei and Dingqishan intrusions in the Liaodong Peninsula for the first time. The detailed analyses of the low-T thermal histories of the Qingchengzi and Wulong orefields and the comparison of the Liaodong and Jiaodong Peninsulas presented here better reflect the evolution of orefields in northeast China. Consequently, the following conclusions can be drawn:

1. The heterogeneous distributions of U and Th and the presence of radiation damage are the main factors responsible for the intra-sample dispersion of ZHe and AHe ages. In contrast, compared with the AHe ages, the cooling rate had a greater effect on the dispersion of the ZHe ages.

2. From 129 to 33 Ma, the average exhumation rate, cooling rate and erosion of the Qingchengzi orefield were 28.7 m/Ma, 1.21 °C/Ma and 2.7 km, respectively. Since 33 Ma, the average exhumation rate, cooling rate and erosion achieved 49.2 m/Ma, 1.47 °C/Ma and 1.6 km, respectively. Hence, the total erosion is estimated to have reached 4.3 km. In the Wulong orefield, the average exhumation rate, cooling rate and erosion were 97.4 m/Ma, 3.61 °C/Ma and 3.1 km, respectively, from 65 to 33 Ma and 49.7 m/Ma, 1.49 °C/Ma and 1.6 km, respectively, after 33 Ma. Hence, the total denudation during the two stages is approximately 4.7 km. The eastern part of the Liaodong Peninsula has been deeper eroded than the western part.

3. The ore-forming depths of the Qingchengzi Pb-Zn deposits and Au-Ag deposits are estimated to be 1.5–3.2 km and 1.0–2.2 km, respectively, and the depth of formation of the Wulong gold deposit is approximately 2.1–3.1 km. The mineralization depth is significantly less than the denudation (4.3 km for the Qingchengzi orefield and 4.7 km for the Wulong orefield), thus implying that the orebodies have been heavily eroded that has reduced their size.

4. The thermal histories of the orefields in the Liaodong and Jiaodong Peninsulas collectively reflect three episodes of cooling in northeast China that occurred during the Early Cretaceous (ca. 135–115 Ma), the end of the Late Cretaceous to the Early Eocene (ca. 70–50 Ma) and the Late Eocene to the Oligocene (ca. 38–26 Ma). It seems likely that the tectonic evolution of the Tan-Lu and Yalujiang fault zones since the Cretaceous may have produced significant effects in the uplift and cooling of the orefields in the two peninsulas.

References

Anderson, J.L., Smith, D.R., 1995. The effects of temperature and fo$_2$ on the Al-in-hornblende barometer. Am. Mineral. 80 (5), 549–559.

Ballentine, C.J., Burgess, R., Marty, B., 2002. Tracing fluid origin, transport and interaction in the crust. Rev. Mineral. Geochem. 47, 539–614.

Ban, F.M., 2010. Geological metallogenic characteristics of Qingchengzi Orefield. Popular Bus. 115, 318–319 (in Chinese).

Benjamin, T.M., Johnson, M.N., Naeser, W.C., 1987. Recent rapid uplift in Bolivian Andes, Evidence from fission track dating. Geology 15, 680–683.

Betsi, B.T., Lentz, D., McInnes, B.I.A., Evans, N.J., 2012. Emplacement ages and exhumation rates for intrusion-hosted Cu–Mo–Sb–Au mineral systems at Freegold Mountain (Yukon, Canada), assessment from U-Pb, ^{40}Ar/^{39}Ar, and (U–Th)/He geochronometers. Earth Sci. 49 (1), 653–670.

Braun, J., 2005. Quantitative Constraints on the rate of landform evolution derived from low-Temperature thermochronology. Rev. Mineral. Geochem. 58 (1), 351–374.

Chang, J., Qiu, N.S., Zuo, Y.H., Li, C.C., 2011. The new evidence on tectonic uplift in kepingtage area, tarim, china: constraints from (U–Th)/He ages. Chin. J. Geophys. 54 (1), 163–172.

Chang, Y., Xu, C.H., Reiners, P.W., Zhou, Z.Y., 2010. The exhumation evolution of the Micang Shan-Hannan uplift since Cretaceous, Evidence from apatite (U-Th)/He dating. Chin. J. Geophys. 53 (4), 912–919.

Chang, Y., Zhou, Z.Y., 2010. Basic methods to inverse exhumation rates using low-temperature thermochronological data. Sci. Technol. Rev. 28 (21), 86–94 (in Chinese with English abstract).

Chen, B.L., 2001. Calculation of metallogenic depth of lode gold deposits from mineralization structure dynamics. Chin. J. Geol. 36 (3), 380–384 (in Chinese).

Chen, J.F., Yu, G., Xue, C.J., Qian, H., He, J.F., Xing, Z., Zhang, X., 2005. Pb isotope geochemistry of Lead, Zinc, Gold and Silver deposit clustered region, Liaodong rift zone, northeastern China. Sci. China Earth Sci. 48 (4), 467–476.

Chen, Q.M., 2013. Ore-forming depth and denudation degree, in the Northwestern Jiaodong Peninsula: Constraint from fluid inclusion and apatite fission track dataset. Master Dissertation. China university of Geosciences, Wuhan pp. 73–74 (in Chinese with English abstract).

Chen, R.D., 1995. On the translation movement of Tan-Lu fracture from geological correlation between East and West Liaoning. Liaoning Geol. 3, 184–193 (in Chinese).

Chen, Y.J., Pirajno, F., Lai, Y., Li, C., 2004. Metallogenic time and tectonic setting of the jiaodong gold province, eastern china. Acta Petrol. Sin. 20 (4), 907–922.

Cottle, J.M., Jessup, M.J., Newell, D.L., Searle, M.P., Law, R.D., Horstwood, M.S.A., 2007. Structural insights into the early stages of exhumation along an orogen-scale detachment: the south Tibetan detachment system, Dzakaa Chu Section, Eastern Himalaya. J. Struct. Geol. 29 (11), 1781–1797.

Deng, J., Wang, C.M., Bagas, L., Carranza, E.J.M., Lu, Y.J., 2015. Cretaceous-Cenozoic tectonic history of the Jiaojia Fault and gold mineralization in the Jiaodong Peninsula, China: constraints from zircon U-Pb, illite K-Ar, and apatite fission track thermo-chronometry. Miner. Deposita 50 (8), 987–1006.

Ding, R.X., Zhou, Z.Y., Wang, W., 2007. Modeling exhumation rates of orogenic belts with Low-temperature thermochronological data. Adv. Earth Sci. 22 (5), 447–455 (in Chinese with English abstract).

Dong, N.T., Wu, G.L., Wang, G.Q., Cao, F.L., 1989. The basic geological features of the Yalujiang fracture belt and the metallogenic regularities. Jilin Geol. 4, 1–25 (in Chinese).

Duan, X.X., Liu, J.M., Wang, Y.B., Zhou, L.L., Li, Y.G., Li, B., Zhang, Z., Zhang, Z.L., 2012. Geochronology, geochemistry and geological significance of Late Triassic magmatism in Qingchengzi orefield, Liaoning. Acta Petrol. Sin. 28 (2), 595–606 (in Chinese with English abstract).

Duan, X.X., Zeng, Q.D., Yang, J.H., Liu, J.M., Wang, Y.B., Zhou, L.L., 2014. Geochronology, geochemistry and Hf isotope of Late Triassic magmatic rocks of Qingchengzi district in Liaoning peninsula, Northeast China. J. Asian Earth Sci. 91, 107–124.

Evans, N.J., Wilson, N.S.F., Cline, J.S., McInnes, B.I.A., Byrne, J., 2005. (U–Th)/He thermochronology of fluorite and the low temperature history of Yucca Mountain, Nevada. Appl. Geochem. 20 (6), 1099–1105.

Fan, H.R., Feng, K., Li, X.H., Hu, F.F., Yang, K.F., 2016. Mesozoic gold mineralization in the Jiaodong and Korean peninsulas. Acta Petrol. Sin. 32 (10), 3225–3238 (in Chinese with English abstract).

Fang, R.H., He, S.S., Fu, D.B., 1994. Nonferrous metallic ore deposit in the east Liaoning–south Jilin early Proterozoic rift. In: Rui, Z.Y., Shi, L.D., Fang, R.H. (Eds.), Geology of Nonferrous Metallic Deposits in the Northern Margin of the North China Landmass and Its Adjacent Area. Geological Publishing House, Beijing, pp. 54–109 (in Chinese).

Farley, K.A., 2000. Helium diffusion from apatite, general behavior as illustrated by Durango fluorapatite. J. Geophys. Res. 105, 2903–2914.

Farley, K.A., Wolf, R.A., Silver, L.T., 1996. The effects of long alpha-stopping distances on (U–Th)/He ages. Geochim. Cosmochim. Acta 60 (21), 4223–4229.

Fitzgerald, P.G., Baldwin, S.L., Webb, L.E., O'Sullivan, P.B., 2006. Interpretation of (U–Th)/He single grain ages from slowly cooled crustal terranes: a case study from

the Transantarctic Mountains of southern Victoria Land. Chem. Geol. 225, 91–120.

Flowers, R.M., 2009. Exploiting radiation damage control on apatite (U–Th)/He dates in cratonic regions. Earth Planet. Sci. Lett. 277, 148–155.

Fu, F.Q., McInnes, B.I.A., Evans, N.J., Davies, P.J., 2010. Numerical modeling of magmatic–hydrothermal systems constrained by U-Th–Pb–He time–temperature histories. J. Geochem. Explor. 106, 90–109.

Grimmer, J.C., Jonckheere, R., Enkelmann, E., Ratschbacher, L., Hacker, B.R., Blythe, A.E., Wagner, G.A., Wu, Q., Liu, S., Dong, S., 2002. Cretaceous – Cenozoic history of the southern Tan-Lu fault zone: apatite fission-track and structural constraints from the Dabie Shan (eastern China). Tectonophysics 359 (3–4), 225–253.

Guo, C.Y., Zhang, W.Z., Ge, L.S., Qing, M., Gao, B.F., Xia, R., 2011. Estimation on Mineralization Depth and Erosion of Gold Deposits in the Northwestern Area of Jiaodong Peninsular. Metal Mine 422, 112–115 (in Chinese).

Guo, H.J., 2006. Geological analysis of nonferrous metal deposit in China and North Korea. World Nonferrous Met. 12, 16–18 (in Chinese with English abstract).

Guo, W.J., Chen, S.L., Yu, H.F., Qu, H.X., Tan, W.G., 2005. The emplacement mechanism and continental dynamics evolution of Indosinian intrusive rocks in east Liaoning Peninsula. Geol. Resour. 14 (2), 92–96 (in Chinese with English abstract).

Hammarstrom, J.M., Zen, E.A., 1986. Aluminum in hornblende, an empirical igneous geobarometer. Am. Mineral. 71, 1297–1313.

He, S., Tao, Y.C., Jiang, P., 1995. Study on geothermal history in swell area of southeast Songliao Basin by using several paleogeothermometers. Earth Sci. 20 (3), 328–334 (in Chinese with English abstract).

Hollister, L.S., Grissom, G.C., Peters, E.K., Stowell, H.H., Sisson, V.B., 1987. Confirmation of the empirical correlation of Al in hornblende with pressure of solidification of calc-alkaline plutons. Am. Mineral. 72, 231–239.

Hu, F.F., Fan, H.R., Jiang, X.H., Li, X.C., Yang, K.F., Mernagh, T., 2013. Fluid inclusions at different depths in the Sanshandao gold deposit, Jiaodong Peninsula, China. Geofluids 13 (4), 528–541.

Hu, F.F., Fan, H.R., Yang, J.H., Wan, Y.S., Liu, D.Y., Zhai, M.G., Jin, C.W., 2004. Mineralizing age of the Rushan lode gold deposit in the Jiaodong Peninsula: Shrimp U-Pb dating on hydrothermal zircon. Chin. Sci. Bull. 49 (15), 1629–1636.

Huang, L., Liu, C.Y., Kusky, T.M., 2015. Cenozoic evolution of the Tan–Lu fault zone (east China)—constraints from seismic data. Gondwana Res. 28 (3), 1079–1095.

Ji, Z.J., 2009. Metallogenic geological characteristics and prospecting direction of Wulong Gold Deposit in Liaoning Province. Chin. Hi-tech Enterp. 1, 141–143.

Jiang, S.Y., Wei, J.Y., 1989. Geochemistry of the Qingchengzi lead-zinc deposit. Mineral deposits 8 (4), 20–28 (in Chinese).

Johnson, M.C., Rutherford, M.J., 1989. Experimental calibration of the aluminum –in -hornblende geobarometer with application to Long Valley caldera (California) volcanic rocks. Geology 17, 837–841.

Ketcham, R.A., 2005. Forward and inverse modeling of low-temperature thermochronometry data. Rev. Mineral. Geochem 58 (1), 275–314.

Kooijman, E., Mezger, K., Berndt, J., 2009. New constraints on Pb diffusion and closure temperature in rutile from in situ U-Pb dating by La-ICP-MS. Geochmica Et Cosmochimica Acta 25 (1), 715–720.

Li, B.L., Wang, L., Huo, L., Zhang, H., 2009. Characteristics and genesis of ore - forming fluids in 52 # veins of Linglong gold mine in Jiaodong. Adv. Nat. Sci. 19 (1), 51–60 (in Chinese with English abstract).

Li, G.M., Cao, M.J., Qin, K.Z., Evans, N.J., McInnes, B.I.A., Liu, Y.S., 2014. Thermal-tectonic history of the Baogutu porphyry Cu deposit, West Junggar as constrained from zircon U-Pb, biotite Ar/Ar and zircon/apatite (U–Th)/He dating. J. Asian Earth Sci. 79, 741–758.

Li, H.M., Shao, X.F., 2015. Comparison on the metallogenic geological conditions of polymetallic deposits between Northern Korean peninsula and Eastern Liaoning province. Geol. Resour. 24 (4), 362–364 (in Chinese with English abstract).

Li, J.W., Ma, C.Q., Vasconcelos, P., Zhou, M.F., Zhao, X.F., 2006. Geochronology of the Pengjiakuang and Rushan gold deposits, eastern Jiaodong Gold Province, Northeastern China: implications for regional mineralization and geodynamic setting. Econ. Geol. 101 (5), 1023–1038.

Li, J.W., Vasconcelos, P.M., Zhang, J., Zhou, M., Zhang, X.J., Yang, F.H., 2003. ^{40}Ar/^{39}Ar constraints on a temporal link between gold mineralization, magmatism, and continental margin transtension in the Jiaodong gold province, eastern china. J. Geol. 111 (6), 741–751.

Li, R.X., Zhang, X.Y., Jin, K.L., 2001. Application of vitrinite reflectance to reconstruction of the tectonic features of the Bohai Gulf Basin. Acta Mineral. Sin. 21 (4), 705–709 (in Chinese with English abstract).

Li, S.Z., Liu, J.Z., Zhao, G.C., Wu, F.Y., Han, Z.Z., Yang, Z.Z., 2004. Key chronology of Mesozoic deformation in the eastern block of the North China Craton and its constraints on regional tectonics, a case of Jiaodong and Liaodong Peninsula. Acta Petrol. Sin. 20 (3), 633–646 (in Chinese with English abstract).

Li, X.D., Chen, R.D., Shan, X.D., Yang, Y.J., Zhan, L.H., Zhang, F.S., 2000. Cover fold and structure evolution of the southern Liaodong Peninsula. Liaoning Geol. 17 (3), 190–198 (in Chinese with English abstract).

Liu, F.X., Qiu, Z.H., Wang, W., Yao, G., 2010. Geological characteristics and genesis of the Wulong Gold Deposit. Sci. Technol. Innovation Herald 10, 48–49 (in Chinese with English abstract).

Liu, G.P., Ai, Y.F., 2002. Study on ore-forming epoch of Xiaotongjiapuzi Gold Depositm, Liaoning Province. Mineral deposits 21 (1), 53–57 (in Chinese with English abstract).

Liu, H.J., Sha, D.X., Li, G.S., 2013. Genetic connection between the Lead-Zinc and Gold-Silver Deposits in the Qingchengzi Ore Concentration Area in Eastern Liaoning. Geol. Resour. 22 (4), 299–303 (in Chinese with English abstract).

Liu, J., 1995. Tectonic deformation texture and ore-controlling features of Qingchengzi orefield, Liaoning Province. Liaoning Geol. 2, 148–157 (in Chinese).

Liu, X., Fan, H.R., Evans, N.J., Batt, G.E., McInnes, B.I.A., Yang, K.F., Qin, K.Z., 2014. Cooling and exhumation of the mid-Jurassic porphyry copper systems in Dexing City,

SE China, insights from geo- and thermochronology. Miner. Deposita 49, 809–819.

Liu, X.L., Jiang, Y., Liu, Z.Y., 2000. Geological characteristics and metallogenic mechanism of Gaojiapuzi large-scale Au-Ag deposits in Qingchenzi orefield. Liaoning Geol. 17 (2), 121–127 (in Chinese with English abstract).

Liu, Z.Y., Xu, X.C., Tian, Y.C., Yang, D.J., Jiang, Y.Z., Tian, S.H., Wei, M., 2007. Relationship between sedimentation-exhalation ore-forming process and gold-silver polymetallic mineralization in Qingchenzi area, Liaoning Province. Mineral Deposits 26 (5), 563–571 (in Chinese with English abstract).

Luo, Y., Sun, M., Zhao, G.C., Li, S.Z., Xu, P., Ye, K., Xia, X.P., 2004. LA-ICP-MS U-Pb zircon ages of the Liaohe Group in the Eastern Block of the North China Craton: Constraints on the evolution of the Jiao-Liao-Ji Belt. Precambr. Res. 134 (3–4), 349–371.

Luo, Y., Sun, M., Zhao, G.C., Li, S.Z., Ayers, J.C., Xia, X.P., Zhang, J.H., 2008. A comparison of U-Pb and Hf isotopic compositions of detrital zircons from the North and South Liaohe Groups, constraints on the volution of the Jiao-Liao-Ji Belt, North China Craton. Precambr. Res. 163, 279–306.

Lv, G.X., Liu, R.X., Wang, F.Z., Ding, T.P., Li, X.B., Chen, J., 2000. A method for estimating the depth of petrogenesis and metallogenesis. J. Geomech. 6 (3), 50–62 (in Chinese with English abstract).

Lv, X.X., 2006. Thermal Evolutional History and Hydrocarbon Accumulation in the Eastern Linqing Depression, Bohai Bay Basin. Chin. J. Geol. 41 (4), 676–687 (in Chinese with English abstract).

McDowell, F.W., McIntosh, W.C., Farley, K.A., 2005. A precise ^{40}Ar/^{39}Ar reference age for the Durango apatite (U–Th)/He and fission-track dating standard. Chem. Geol. 214 (3–4), 249–263.

McInnes, B.I.A., Evans, N.J., Fu, F.Q., Garwin, S., Belousova, E., Griffin, W.L., Bertens, A., Sukarna, D., Permanadewi, S., Andrew, R.L., Deckart, K., 2005. Thermal history analysis of selected Chilean, Indonesian and Iranian porphyry Cu-Mo-Au deposits. In: In: Porter, T.M. (Ed.), Superporphyry Copper and Gold Deposits-a Global Perspective Adelaide PGC Publishing, pp. 42.

McInnes, B.I.A., Farley, K.A., Sillitoe, R.H., Kohn, B., 1999. Application of (U–Th)/He dating to the estimation of the sense and amount of vertical fault displacement at the Chuquicamata Mine, Chile. Econ. Geol. 94, 937–948.

Qiu, Y.M., Groves, D.I., Mcnaughton, N.J., Wang, L.G., Zhou, T.H., 2002. Nature, age, and tectonic setting of granitoid-hosted, orogenic gold deposits of the Jiaodong Peninsula, Eastern North China Craton, China. Miner. Deposita 37 (3), 283–305.

Reiner, P.W., Nicolescu, S., 2006. Measurement of parent nuclides for (U-Th)/He chronometry by solution sector ICP-MS. Arhdl Report 1, http://www.geo.arizona.edu/~reiners/arhdl/arhdl.com.

Reiners, P.W., Farley, K.A., 1999. Helium diffusion and (U–Th)/He thermochronometry of titanite. Geochim. Cosmochim. Acta 63 (22), 3845–3859.

Reiners, P.W., Farley, K.A., 2001. Influence of crystal size on apatite (U-Th)/He thermochronology: An example from the Bighorn Mountains, Wyoming. Earth Planet. Sci. Lett. 188, 413–420.

Reiners, P.W., Nicolescu, S., 2006. Measurement of parent nuclides for (U–Th)/He chronometry by solution sector ICP-MS. ARHDL Rep. 1 (http://www.geo.arizona.edu/~reiners/arhdl/arhdl.htm).

Reiners, P.W., Spell, T.L., Nicolescu, S., Zanetti, K.A., 2004. Zircon (U–Th)/He thermochronometry, He diffusion and comparisons with ^{40}Ar/^{39}Ar dating. Geochim. Cosmochim. Acta 68, 1857–1887.

Ren, Z.L., Xiao, D.M., Chi, Y.L., 2001. Restoration of the palaeogeotherm in Songliao Basin. Petrol. Geol. Oilfield Dev. Daqing 20 (1), 13–14 (in Chinese).

Rui, Z.Y., Shi, L.D., Fang, R.H., 1994. Geology of Nonferrous Metallic Deposits in the Northern Margin of North China Landmass and Its Adjacent Area. Geological Publishing House, Beijing pp. 66-67, 518-519 (in Chinese).

Sang, H.Q., Wang, S.S., Hu, S.L., Qiu, J., 1992. Closure temperature and ^{40}Ar/^{39}Ar age spectrum of biotites from Mangshan granodiorite tonalite in Qian'an County, Hebei Province. Acta Petrol. Sin. 8 (4), 332–340 (in Chinese with English abstract).

Scharf, A., Handy, M.R., Schmid, S.M., Favaro, S., Sudo, M., Schuster, R., Hammerschmidt, K., 2016. Grain-size effects on the closure temperature of white mica in a crustal-scale extensional shear zone – implications of in-situ ^{40}Ar/^{39}Ar laser-ablation of white mica for dating shearing and cooling (Tauern Window, Eastern Alps). Tectonophysics 674, 210–226.

Schmidt, M.W., 1992. Amphibole composition in tonalite as a function of pressure, an experimental calibration of the Al-in-hornblende barometer. Contrib. Miner. Petrol. 110, 304–310.

Schumacher, J.C., 1997. Appendix2: The estimation of ferriciron in the electron-microprobe analysis of amphiboles. Can. Mineral. 35, 219–246.

Scott, D.J., Stonge, M.R., 1995. Constraints on Pb closure temperature in titanite based on rocks from the Ungava orogen, Canada: implications for U-Pb geochronology and P-T-t path determinations. Geology 23 (12), 1123–1126.

Shao, J.L., 1988. The mineralogy of prospecting Gold Deposits. China University of Geosciences Press, Beijing pp. 1-158 (in Chinese).

Shuster, D.L., Flowers, R.M., Farley, K.A., 2006. The influence of natural radiation damage on helium diffusion kinetics in apatite. Earth Planet. Sci. Lett. 249, 148–161.

Song, J.C., Hu, T.J., Wang, E.D., Jia, S.S., 2009. A comparison of metallogenic conditions between two sides of Yalu River and its inspiration to future ore-prospecting in Liaodong area. Mineral Deposits 28 (4), 449–461 (in Chinese with English abstract).

Spencer, A., Kohn, B., Gleadow, A., Norman, M., Belton, D., Carter, T., 2004. The importance of residing in a good neighbourhood, rechecking the rules of the game for apatite (U-Th)/He thermochronology. In: In: Andressien, P. (Ed.), 10th International Fission Track Dating, Amsterdampp. 20.

Spiegel, C., Kohn, B., Belton, D., Berner, Z., Gleadow, A., 2009. Apatite (U–Th–Sm) /He thermochronology of rapidly cooled samples, the effect of He implantation. Earth Planet. Sci. Lett. 285 (1–2), 105–114.

Stockli, D.F., Farley, K.A., Dumitru, T.A., 2000. Calibration of the apatite (U–Th)/He thermochronometer on an exhumed fault block, White Mountains, California.

Geology 28, 983–986.

Sun, F.Y., Jin, W., Li, B.L., 2000. Considerations on the mineralizing depth of hydrothermal lode gold deposits. J. Changchun Univ. Sci. Technol. 30, 27–30 (in Chinese with English abstract).

Sun, H.S., Li, H., Liu, L., Chen, Q.M., Yang, H., Wu, P., 2016. Exhumation history of the Jiaodong and its adjacent areas since the late Cretaceous: Constraints from low temperature thermochronology. Sci. China Earth Sci. 60 (3), 531–545.

Sun, H.Y., Sun, W.T., 2004. The comparison of study premises between Liaohe Group sidious deposit controlled by strata of Liaoning Eastern Middle part and Jiande Pattern Deposit of Korea and perspective forecast. Non-ferrous Min. Metall. 20 (4), 9–13 (in Chinese with English abstract).

Sun, J.B., Sun, T.F., Chen, W., Yu, S., Yin, J.Y., Li, C., Zhang, Y., Liu, X.Y., 2015. Thermotectonic evolution history of Hongyuntan area, eastern Tianshan, Xinjiang, Constrained from $^{40}Ar/^{39}Ar$ and (U-Th) /He dating. Acta Petrol. Sin. 31 (12), 3732–3742.

Sun, M., Riehard, L.A., Riehard, S.J.L., Jiang, C.C., Wu, J.H., 1993. Petrochemistry and Sr, Pb and Nd isotopic geochemistry of the Paleoproterozoic Kuandian Complex the eastern Liaoning Province, China. Precambr. Res. 62 (1–2), 171–190.

Sun, X.M., Wang, S.Q., Wang, Y.D., Du, J.Y., Xu, Q.W., 2010. The structural features and evolutionary series in the northern segment of Tancheng-Lujiang fault zone. Acta Petrol. Sin. 26 (1), 165–176.

Tagami, T., Farley, K.A., Stockli, D.F., 2003. (U–Th)/He geochronology of single zircon grains of known Tertiary eruption age. Earth Planet. Sci. Lett. 207 (1–4), 57–67.

Wan, B., Jia, L.H., Dai, Y.L., Suo, R., 2013. Moderate-strong earthquakes and their tectonic correlation in the Liaodong Peninsula. Seismolog. Geol. 35 (2), 300–314 (in Chinese with English abstract).

Wan, Y.S., Song, B., Liu, D.Y., Wilde, S.A., Wu, J.S., Shi, Y.R., Yin, X.Y., Zhou, H.Y., 2006. SHRIMP U-Pb zircon geochronology of Paleoproterozoic metasedimentary rocks in the North China Craton, Evidence for a major Late Paleoproterozoic tectonothermal event. Precambr. Res. 149, 249–271.

Wang, F., Feng, H.L., Shi, W.B., Zhang, W.B., Wu, L., Yang, L.K., Wang, Y.Z., Zhang, Z.G., Zhu, R.X., 2016. Relief history and denudation evolution of the northern Tibet margin, Constraints from $^{40}Ar/^{39}Ar$ and (U–Th)/He dating and implications for far-field effect of rising plateau. Tectonophysics 675, 196–208.

Wang, F., Zhou, X.H., Zhang, L.C., Ying, J.F., Zhang, Y.T., Wu, F.Y., Zhu, R.X., 2006. Late mesozoic volcanism in the great Xing'an Range (NE china): timing and implications for the dynamic setting of NE Asia. Earth Planet. Sci. Lett. 251 (1–2), 179–198.

Wang, J.P., Zhai, Y.S., Liu, J.J., Liu, Z.J., Liu, J., 2008. A new approach to post-ore change and preservation of ore deposits, Fission Track analysis. Adv. Earth Sci. 23 (4), 427–428 (in Chinese with English abstract).

Wang, K.Y., Qing, M., Bian, H.Y., Wan, D., Sun, F.Y., Liu, Z.H., Ji, Z.J., 2010. The geological features and geochemistry of ore-forming fluids of Wulong Gold Deposit in Liaoning Province. J. Jilin Univ. 40 (3), 557–564 (in Chinese with English abstract).

Wang, X.F., Liu, P.D., Yang, G.L., Zhang, X.M., Yi, X., 2010. Analyzing the geological features of the Qingchengzi Pb-Zn orefield. Non-Ferrousmining Metall. 26 (2), 2–6 (in Chinese).

Wei, J.H., Liu, C.Q., Li, Z.D., Zhao, Y.X., 2003. U-Pb, Rb-Sr isotopic dating of diagenesis and mineralization of Gold Deposits in the Dandong area. Acta Geol. Sin. 77 (1), 113–119 (in Chinese with English abstract).

Wei, J.H., Liu, C.Q., Zhao, Y.X., Li, Z.D., 2001. Time span of the major ore-forming stages of the Wulong Gold Deposit, Liaoning. Geolog. Rev. 47 (4), 433–437 (in Chinese with English abstract).

Wei, J.H., Qiu, X.P., Guo, D.Z., Tan, W.J., 2004. Geochemistry of ore fluids and Rb-Sr isotopic dating for the Wulong Gold Deposit in Liaoning, China. Acta Geol. Sin. 78 (6), 1267–1274 (in Chinese with English abstract).

Wolf, R.A., Farley, K.A., Kass, D.M., 1998. Modeling of the temperature sensitivity of the apatite (U–Th)/He thermochronometer. Chem. Geol. 148, 105–114.

Wolf, R.A., Farley, K.A., Silver, L.T., 1996. Helium diffusion and low-temperature thermochronometry of apatite. Geochim. Cosmochim. Acta 60 (21), 4231–4240.

Wolf, R.A., Farley, K.A., Sliver, L.T., 1997. Assessment of (U-Th)/He thermochronometry, The low-temperature history of the San Jacinto Mountains. Calif. Geol. 25 (1), 65–68.

Wu, F.Y., Yang, J.H., Liu, X.M., 2005. Geochronological framework of the Mesozoic granitic magmatism in the Liaodong Peninsula, Northeast China. Geol. J. China Univ. 11 (3), 305–317 (in Chinese with English abstract).

Wu, L., Monié, P., Wang, F., Lin, W., Ji, W.B., Bonno, M., Münch, P., Wang, Q.C., 2016. Cenozoic exhumation history of Sulu terrane: Implications from (U–Th)/He thermochrology. Tectonophysics 672–673, 1–15.

Xia, H.K., Xu, D.M., 1993. Features of Yalujiang River Fault (south segment) activity and seismicity. J. Seismol. Res. 16 (4), 391–400 (in Chinese).

Xiao, G.L., Liu, T.X., Zhang, G.X., 2003. Probing into the origin and mineralization model of Wulong Gold Deposit, Liaoning Province. Gold 24 (11), 17–20.

Xue, C.J., Chen, Y.C., Lu, Y.F., Li, H.Q., 2003. Metallogenic epochs of Au and Ag deposits in Qingchengzi ore-clustered area, Eastern Liaoning Privince. Mineral deposits 22 (2), 177–184 (in Chinese with English abstract).

Yang, F.C., Song, Y.H., Zhang, P., Chai, P., Li, B., 2016. Forming fluid characteristics and tracing of the ore-forming source materials of gold-silver deposits in the Qingchengzi ore concentration area. Acta Geol. Sin. 90 (10), 2775–2785.

Yang, L., Yang, G.S., Tian, P., Sun, B.D., 2015. Application of (U-Th)/He dating technique in historical evolution studies of deposits. Value Eng. 17, 202–205 (in Chinese).

Yang, L.Q., Deng, J., Wang, Z.L., Zhang, L., Guo, L.N., Song, M.C., Zheng, X.L., 2014. Mesozoic gold metallogenic system of the Jiaodong gold province, eastern China. Acta Petrol. Sin. 30 (9), 2447–2467.

Yu, G., Chen, J.F., Xue, C.J., 2009. Geochronological framework and Pb, Sr isotope geochemistry of the Qingchengzi Pb-Zn-Ag-Au orefield, Northeastern China. Ore Geol. Rev. 35, 367–382.

Zeitler, P., 1985. Closure temperature implications of concordant $^{40}Ar/^{39}Ar$ potassium feldspar and zircon fission-track ages from high-grade terranes. Nucl. Tracks Radiat. Meas. 10 (3) 441-441.

Zhai, Y.S., Deng, J., Peng, R.M., 2000. Research contents and methods for post-ore changes, modifications and preservation. Earth Sci. 25 (4), 340–345 (in Chinese with English abstract).

Zhang, G.R., Jiang, S.E., Han, X.P., Huang, Z.F., Qu, H.X., Guo, W.J., Wang, F.J., 2006. The main characteristics of Yalujiang Fault Zone and its significance. Geol. Resour. 15 (1), 11–19 (in Chinese with English abstract).

Zhang, H.Y., Wu, H., Zhao, H.L., 2012. Comparative Study on Pb - Zn Deposit in Qingchengzi, Liaoning Province and North Korea. Modern Mining 1, 54–57 (in Chinese with English abstract).

Zhang, J.D., Hao, T.Y., Dong, S.W., Chen, X.H., Cui, J.J., Yang, X.Y., Liu, C.Z., Li, T.J., Xu, Y., Huang, S., Re, F.L., 2015. The structural and tectonic relationships of the major fault systems of the Tan-Lu fault zone, with a focus on the segments within the North China region. J. Asian Earth Sci. 110, 85–100.

Zhang, L., Li, G.W., Zheng, X.L., An, P., Chen, P.Y., 2016. $^{40}Ar/^{39}Ar$ and Fission Track dating constraints on the tectonothermal history of the world class Sanshandao gold deposit, Jiaodong Peninsula, eastern China. Acta Petrol. Sin. 32 (8), 2465–2476 (in Chinese with English abstract).

Zhang, Y.Q., Dong, S.W., Shi, W., 2003. Cretaceous deformation history of the Tan–Lu fault zone in Shandong province, eastern China. Tectonophysics 363 (3), 243–258.

Zhang, Y.Q., Dong, S.W., 2008. Mesozoic tectonic evolution history of the Tan-Lu fault zone, China: Advances and new understanding. Geol. Bull. China 27 (9), 1371–1390.

Zhao, F.Y., 2015. Study on apatite and zircon fission-track of early Cretaceous granite of Sanfoshan in Jiaodong. Master Thesis. China University of Geosciences, Beijing (in Chinese with English abstract).

Zhao, G.F., Sun, L.M., 1997. Geology and ore forming mechanism of the Xiaotongjiapuzi gold deposit, Qingchengzi. Geol. Explor. Non-ferrous Met. 6 (4), 212–217 (in Chinese).

Zhou, G.F., Lv, G.X., Deng, J., Shen, Y.K., Guo, T., 2008. Study on the fluid inclusions characteristics of the Sanshandao Gold Deposit, Shandong Province, China and its geological significance. Geosciences 22 (1), 24–33 (in Chinese with English abstract).

Zhu, G., Wang, D.X., Liu, G.S., Niu, M.L., Song, C.Z., 2004. Evolution of the Tan-Lu fault zone and its responses to plate movements in west Pacific basin. Chin. J. Geol. 39 (1), 36–49.

Zhu, G., Wang, W., Gu, C.C., Zhang, S., Liu, C., 2016. Late Mesozoic evolution history of the Tan-Lu Fault Zone and its indication to destruction processes of the North China Craton. Acta Petrol. Sin. 32 (4), 935–949.